博 士 論 文

Research on Two Dimensional Silicon Photonic Resonators for Label Free Detection of Biomaterials

非標識生体物質検出のための二次元シリコン光共振器の研究

Amrita Kumar Sana

広島大学大学院先端物質科学研究科

Graduate School of Advanced Sciences of Matter
Hiroshima University

March 2017

目　　次
（Table of Contents）

主　論　文
（Main Thesis）

Abstract

Early detection as well as identification of biomolecules is very important for the medical diagnosis of many diseases. The mostly used biomaterial detection methods are fluorescence based detection and label-free detection. Fluorescence based detection is quite sensitive and able to detect down to a single molecule and usually use fluorescence tag to identify the target presence. But most complexity is the labeling steps beyond the isolation of target analyses. In contrast, the label free detection performs the detection of biomolecules in their original form also able to easier and cheaper bio detection. In contrast, biosensors such as enzyme-linked immunosorbent assay (ELISA) and surface-plasmon-resonator (SPR) which are already in commercially available label free detection method. However, the advantages of ELISA method need large volume of analytes, expensive and long measurements time. On the other hand the size of SPR is quite large.

Our research focused on Si photonic crystal resonator based biosensor which is compact and highly sensitive because the light of certain frequencies is confined in resonator and takes interaction with biomaterial many times. Thus it has the advantages of being very high sensitive even though the very small volume of analytes.

To confirm our device performance we first used sucrose solution (solution of sugar and water) because of there is no need any extra binding method between device surface and sucrose solution and it is easy to remove them from the device surface. We were able to detect the resonance wavelength shift by changing the sucrose concentration. We reported Q and sensitivity are 10^5 (Q is defined as λ_{res}/FWHM, where λ_{res} is the resonance wavelength and FWHM is full width at half maximum of resonance peak), 1570 nm/RIU (Refractive Index Unit) (sensitivity is the ration of $\Delta\lambda_{res}/\Delta n$, where $\Delta\lambda_{res}$ is a resonance wavelength shift and Δn is a change in refractive index) respectively.

We also made double nanocavity type photonic crystal resonators where surrounding air hole radius were modulated and we got the highest Q of $\sim 2 \times 10^5$, sensitivity of 1571 nm/RIU (s) and minimum detection limit of $< 10^{-6}$ RIU (detection limit is defined as λ_{res}/QS, where Q is the quality factor and S is the sensitivity).

To detect prostate specific antigen (PSA) we used a very special feature called Si binding protein (Si-tag) which has been developed by Professor Akio Kuroda,

Department of Molecular Biotechnology, Hiroshima University. Si-tag immobilizes the receptor anaytes on the device surface (on Si / SiO_2) with a same aligned orientation. Due to the receptor analytes, antigen-antibody is attached on the device surface in an aligned manner and light-matter interaction improves more, as results resonant peak shift even though the concentration is very low. We successfully detected PSA concentration as low as 0.01 ng/mL, where the practical sensitivity is 1 ng/mL.

We describe the mechanism and solution for dominating temperature effects on refractive index based Si optical resonator sensor such as ring resonator and photonic crystal resonator sensors. The temperature change affects the silicon refractive index and affects resonator mechanical shape also. As a result, it is reported that the refractive index change is dominating whereas the mechanical deformation effect is negligible. We also demonstrated that the differential operation is effective to suppress the temperature effect for Si ring resonator sensor.

Dedication

I dedicate this dissertation to my parents and parents-in-laws.

Contents

Chapter 1 Introduction

1.1 Introduction

1.1.1 Background of research

Early detection as well as identification of biomolecules is very important for the medical diagnosis of many diseases. The mostly used biomaterial detection methods are fluorescence based detection and label-free detection.[1)] Fluorescence based detection is quite sensitive and able to detect down to a single molecule and usually use fluorescence tag to identify the target presence. But most complexity is the labeling steps beyond the isolation of target analyses. In contrast, the label free detection performs the detection of biomolecules in their original form also able to easier and cheaper bio detection. In contrast, biosensors such as enzyme-linked immunosorbent assay (ELISA)[2)] and surface-plasmon-resonator (SPR),[3-6)] which are already in commercially available label free detection method. However, the advantages of ELISA method need large volume of analytes, expensive and long measurements time. On the other hand the size of SPR is quite large.

Our research focused on Si photonic crystal resonator based biosensor which is compact and highly sensitive because the light of certain frequencies is confined in resonator and takes interaction with biomaterial many times. Thus it has the advantages of being very high sensitive even though the very small volume of analytes.

1.1.2 Properties of periodic photonic crystal

Photonic crystals[7,8)] are periodic nanostructures with a spatial periodicity in their dielectric constant. Under certain conditions, photonic crystals can create a photonic bandgap, i.e. a certain frequency of light in which propagation through the crystal is inhibited. Light propagation in a photonic crystal is similar to the propagation of electrons and holes in a semiconductor. The periodicity of the electronic potential in semiconductors, which is due to the regular arrangement of atoms in a lattice, gives rise to the electronic bandgaps, which are forbidden energy bands for electrons. Similarly, the periodicity of the refractive index gives rise to photonic bandgaps, forbidden energy

bands for photons. According to the periodicity, photonic crystal are classified into three ways i) one-dimensional (1D) ii) two dimensional (2D) and iii) three dimensional (3D) photonic crystal.

One dimensional photonic crystal:

A one-dimensional photonic crystal (1D PhC), which is a periodic nanostructure with a refractive index distribution along one direction. As illustrated in Fig. 1.1 the simples structures of one dimensional photonic crystal. Because of its wavelength selective reflection properties, can be used in a wide range of applications including Fabry-Perot cavities, optical filter, high efficiency mirrors and distributed feedback laser. Most recently 1D PhCs is also be using as fiber Bragg gratting (FBG), where fiber core refractive index is changing along its axis.

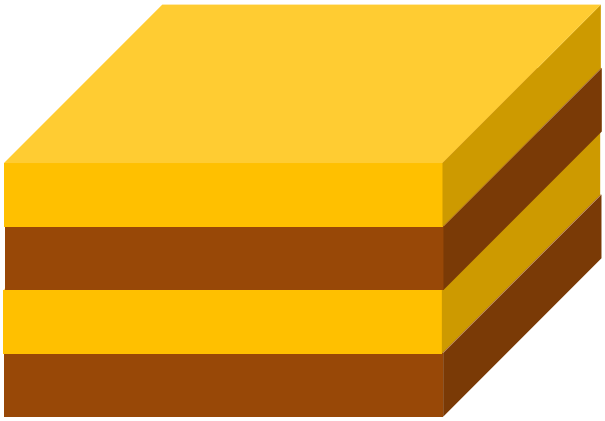

Fig. 1.1. Schematic of one dimensional photonic crystal.

Two dimensional photonic crystal:

The schematic structure of two dimensional (2D) photonic crystals is shown in Fig.1.2. In 2D PhCs, the periodicity of dielectric constant varies along the two axis rather than one direction.

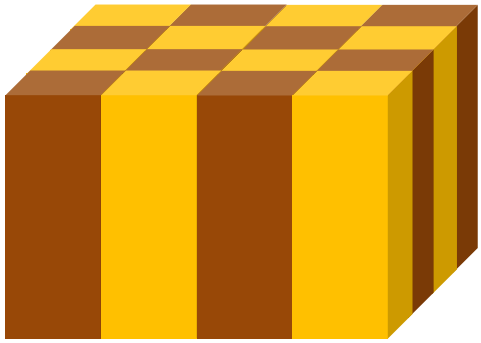

Fig. 1.2. Schematic of two dimensional photonic crystal.

Three dimensional photonic crystal:

In three dimensional (3D) photonic crystal lattice, the dielectric constant varies in all three direction. 3D PhCs is the most challenging structures to fabricate. Waveguiding and making defects in 3D structures has not progressed as like 2D structures and need complex geometry to get 3D bandgaps. The schematic structure of 3D PhCs is shown in Fig. 1.3.

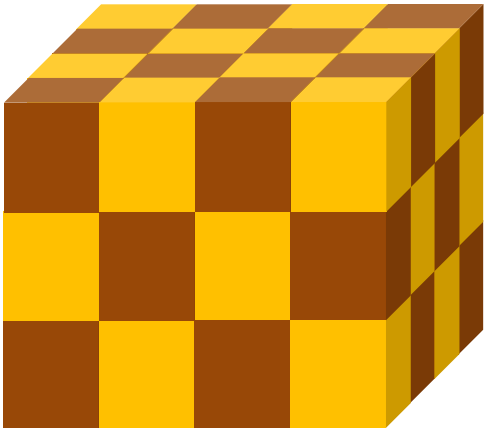

Fig. 1.3. Schematic of three dimensional photonic crystal.

1.1.3 Silicon photonic crystal as biosensor

Photonic crystal based devices that are used for sensing applications are typically micro-fabricated periodic structures on silicon on insulator (SOI) chip. The structures can be designed to exhibit a two-dimensional photonic band gap (PBG) and tune by varying the structural parameters such as lattice constant, air holes radius. In our case, we systematically introduced cavity/defects into the perfect hexagonal lattice during the fabrication process. The cavity was introduced by enlarging radius of the center hole whereas defect was created by removing center hole. Such type cavities typically exhibits small modal volumes as well as strongly localize the electric field in the cavity or defect region is highly sensitive as changes of local refractive index. These properties make them highly interesting for refractive index and biosensing applications. Whilst the sensitivity of that structures are dependent on the precise cavity geometry.

1.2 Goal of this work

In this PhD research work, photonic crystal resonators has been investigated to use as a biosensor. The target of this work was to detect biomaterials i.e prostate specific antigen (PSA) marker at a very lower concentration (below 1ng/mL). We also studied temperature effects on resonance wavelength shift and the solution to avoid the temperature effects by differential silicon ring resonator sensor.

1.3 Dissertation outline

Chapter 1 explains the background of this thesis work. The basic of the photonic crystals, classification and its use as biosensors are described in this section. In Chapter 2 FDTD analysis, design rules of photonic crystals resonators and the theory of resonance wavelength shift are described. Chapter 3 describes the fabrication process and experimental method as well. In Chapter 4 device performance was measured using sucrose solution and prostate specific antigen. The sensitivity and quality factor of the devices are explained in this section. Chapter 5 explains the antigen-antibody reaction process, experimental data and the Langmuir's fitting of the experimental results. In Chapter 6 theory of temperature effects on resonance wavelength of silicon photonic resonators (i.e Si ring and Photonic crystal resonators) are explained. The device

mechanical deformation due temperature rise is also explained. Differential ring resonator sensor was described in this section to avoid the temperature effects. In Chapter 7 the device performances are summarized and compare with other biosensors. The impact of this thesis is described here in this section.

References

[1] F. Hosseinibalam, S. Hassanzadeh, A. Ebnali-Heidari, and C. Karnutsch, Appl. Opt. **51** (2012) 568.

[2] R. M. Lequin, Clin Chem. **51** (2005) 2415.

[3] B. Liedberg, I. Lundstrom, and E. Stenberg, Sens. Actuat. **B I I** (1993) 63.

[4] J. N. Anker, W. P. Hall, O. Lyandres, N. C. Shah, J. Zhao, and R. P. Duyne, Nat. Mat. **7** (2008) 442.

[5] R. Karlsson, J. Mol. Recog. **17** (2004) 151.

[6] C. Caucheteur, Y. Shevchenko, L. Shao, M. Wuilpart, and J. Albert, Opt. Express. **19** (2011) 1656.

[7] S. John, Phys. Rev. Lett. **58** (1987) 2486.

[8] E.Yablonovitch, Phys. Rev. Lett. **58** (1987) 2059.

Chapter 2 Si photonic crystal resonator biosensor

2.1 Finite-Difference-Time-Domain analysis of the photonic crystal resonators

The finite-difference-time-domain[1)] (FDTD) method and the refractive index approach were used for the simulation of photonic crystal resonator device including the band diagrams calculation, characteristics of resonant frequency, field distribution and *Q* factor. The entire simulation process was carried out using RSoft FullWAVE™simulation software. The lattice parameters (such as lattice constant *a*, air hole radius *r*) of the PhC structure were varied to fit the resonant peak within the 1.3 μm wavelength.

2.2 Designing of photonic crystal resonator

The lattice constant *a*, and air hole radius *r* are the key parameters of the photonic crystal resonator based device. After confirming the lattice constant, then air hole radius is calculated by $r = 0.3a$. The input/output waveguide are created by omitting a single row PhC air holes and width of waveguide should be about $\sqrt{3}\,a$. To design the proposed device, we were used L-Edit v16.0 layout. Figure 2.1 shows the layout of device structure.

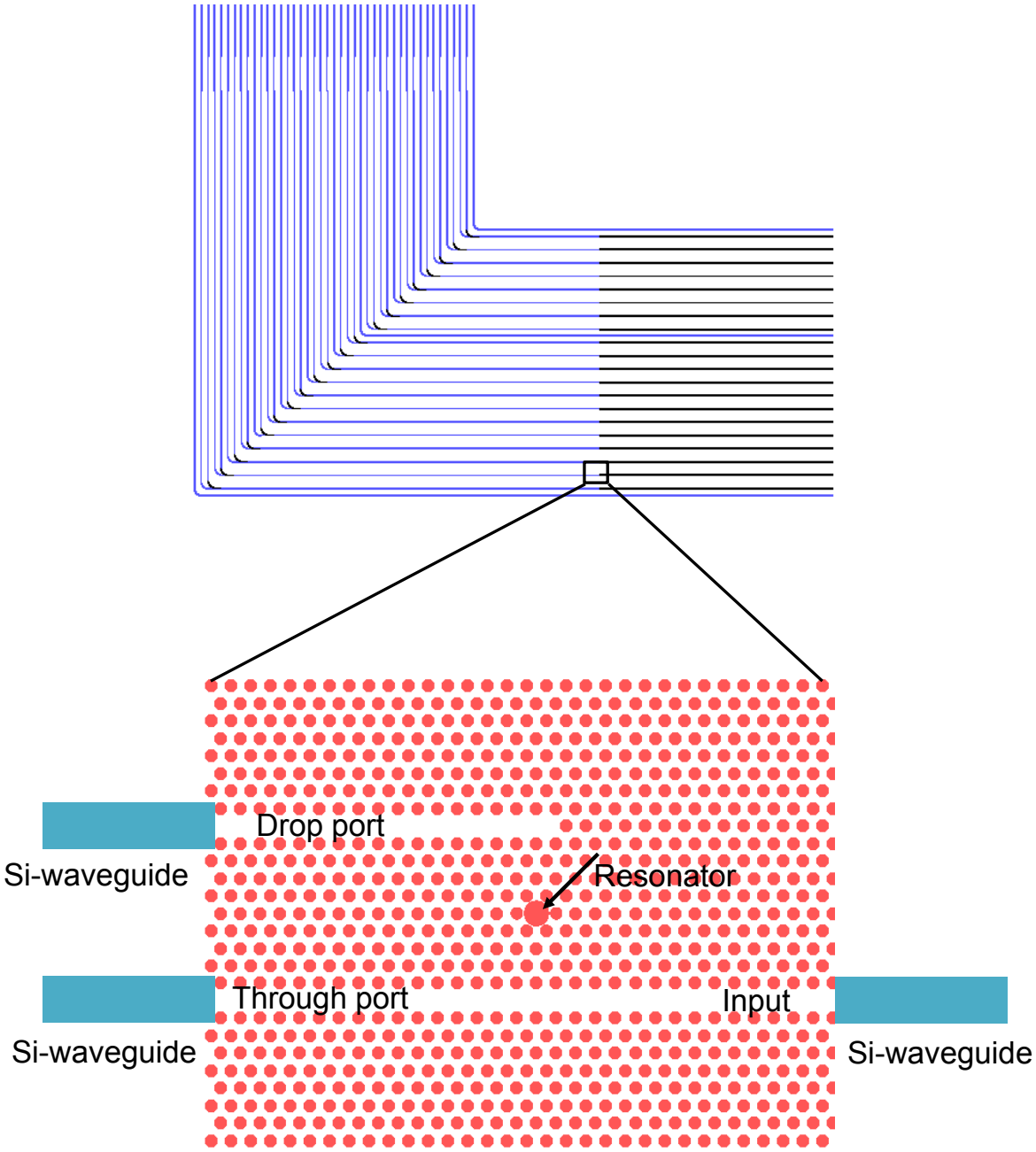

Fig. 2.1. Design layout of PhC cavity resonator.

2.2.1 Cavity type resonator

The cavity type resonator was made by increasing the radius of the center air hole of hexagonal lattice structure. The large resonator area helps to maximize the light and biomolecule interaction. The Schematic of cavity type PhC resonator is shown in Fig. 2.2.

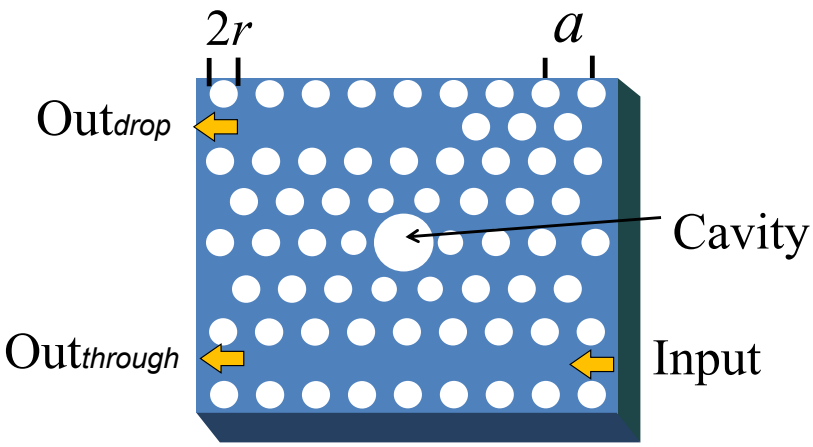

Fig. 2.2. Schematic of cavity type PhC resonator.[9)]

2.2.2 Defect type resonator

The Schematic of cavity type[2-8)] PhC resonator is shown in Fig. 2.3. The defect is made by omitting the center air hole of structure. However, in the defect type structure only evanescent light is in the resonator region and it interacts with biomolecules.

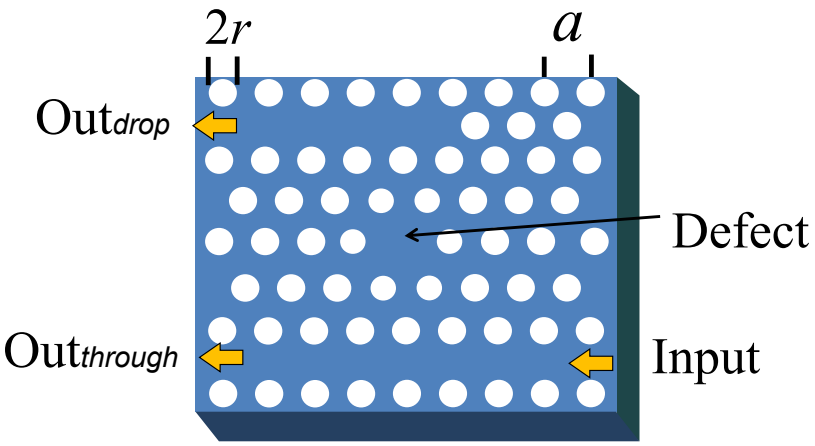

Fig. 2.3. Schematic structure of defect type PhC resonator.[9)]

2.2.3 Special shape resonator (cavity connected with surrounding air holes)

As the design values of any structures substantially increase a bit after the electron beam lithography. The special shape structure is just the connection of surrounding holes and cavity each other. The schematic structure is shown in Fig. 2.4.

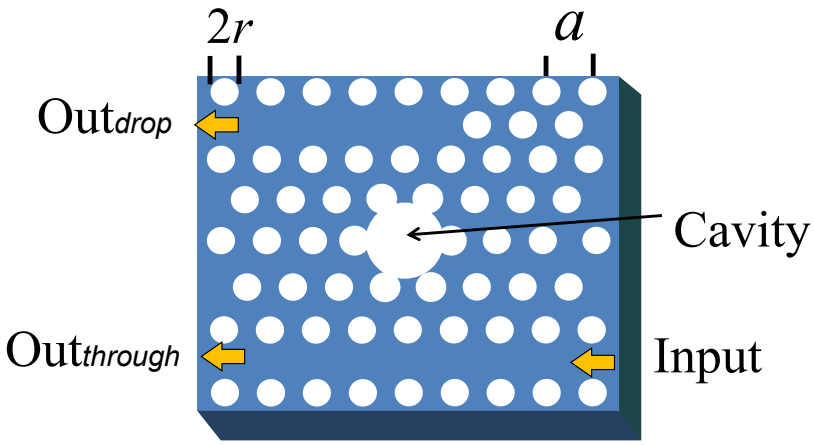

Fig. 2.4. Schematic structure of special shape PhC resonator.

2.2.4 Double cavity resonators with neighbor hole modulation

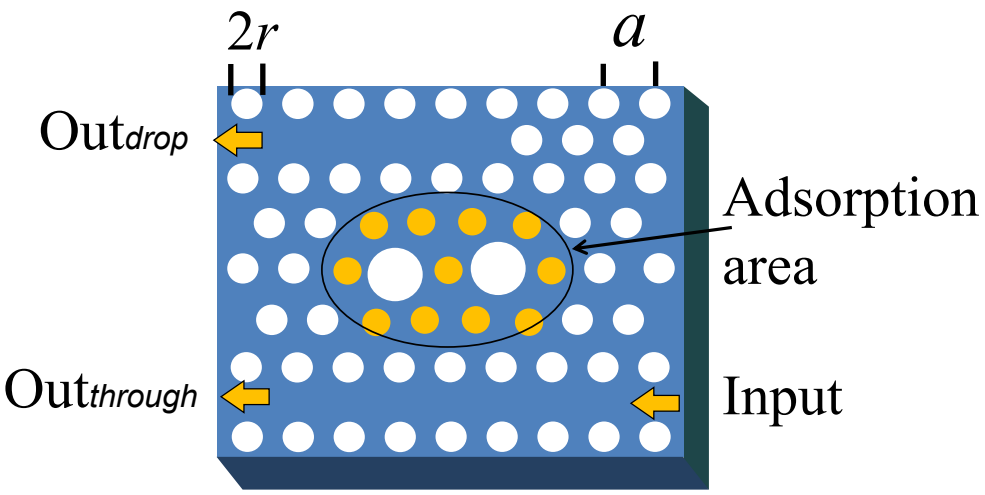

Fig. 2.5. Schematic structure of double cavity PhC resonator.

The double cavity resonator with neighbor hole modulation is shown in Fig. 2.5. As for the large cavity resonator area, much light-biomaterial interaction is possible because electric field distribution is maximum in the modulated air hole region.

2.3 Resonance characteristics of the device

As discussed in the above for both the structures of the cavity and defect-type PhC resonators, the sensing depends on the cavity and defect areas and the effective refractive index change induced by adsorbed biomaterials. The device operation is explained by the following equation:[10)]

$$\lambda_{res} = \frac{n_{eff} L}{m} \tag{2.1}$$

where λ_{res} is the resonance wavelength, n_{eff} is the effective refractive index, L is the size of the resonator, and m (= 1 in the fundamental mode) is an integer. The resonator size L seems to be roughly equal to the length of the defect region for the defect-type; for the cavity-type, L may be the sum of the diameter of the center hole and the size of the remaining defect region.

The shift of resonance wavelength $\Delta\lambda_{res}$ when ambient refractive index changed and is expressed by the following equation:[10)]

$$\Delta\lambda_{res} = \frac{\lambda_{res}\Delta n_{eff}}{n_{eff}} \tag{2.2}$$

where Δn_{eff} is the effective refracitve index of cavity/defect region.

2.4 Details about Q-factor, sensitivity, figure of merit and detection limit

Q-factor:

The quality factor Q of resonation, which is defined by the following equation:

$$Q = \frac{\lambda_{res}}{FWHM} \tag{2.3}$$

where is the resonance wavelength and FWHM is the full width at half maximum of the resonance wavelength.

Sensitivity:

The sensitivity of PhC resonator biosensor is calculated by following equation:

$$S = \frac{\Delta\lambda_{res}}{\Delta n} \tag{2.4}$$

where $\Delta\lambda_{res}$ is the shift of resonance peak and Δn is the change of ambient refractive index of resonator area.

Figure of merit (FOM):

The figure of merit is defined by the following equation:

$$FOM = S \times \frac{Q}{\lambda_{res}} \tag{2.5}$$

where S the sensitivity, Q is the quality factor and λ_{res} is the resonance wavelength.

Detection limit (DL):

In order to analyze the sensor performance quantitatively, the detection limit[11] of the PhC resonator sensor is calculated by the sensitivity S, quality factor Q and the resonance wavelength. The equation is as follows:

$$DL = \frac{\lambda_{res}}{QS}. \tag{2.6}$$

2.5 Comparison of Q value between cavity and defect type structure

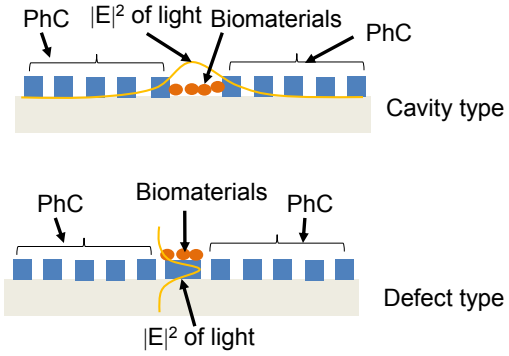

Fig. 2.6. Schematic of light matter interaction in cavity and defect type.

The front schematic view of cavity and defect type is shown in Fig. 2.6. In the defect type, the evanescent part of light interacts with biomaterials, whereas cavity light intensity large inside the cavity region. As for the concentrated electric field, the high Q and larger resonance wavelength shift is possible by cavity type device.

References

[1] J. D. Joannopoulos, S. G. Johnson, J. N. Winn, and R. D. Meade, "Photonic crystal: Molding the flow of light" Princeton University Press, 2007, ISBN:978-0-691-12456-8.

[2] X. Fan, I. M. White, S. I. Shopova, H. Zhu, J. D. Suter, and Y. Sun, Anal. Chem. Act. **620** (2008) 8.

[3] S. Olyaee and A. Naraghi, Phot. Sens. **3** (2013)131.

[4] S. Olyaee, A. Naraghi, and V. Ahmadi, Optik **125** (2014) 596.

[5] S. Olyaee and A. A. Dehghani, Phot. Sens. **2** (2012) 92.

[6] S. Olyaee and A. A. Dehghani, Sens. Lett. **11** (2013)1854.

[7] S. Olyaee and M. Azizi, Phot. Sens. **4** (2014) 220.

[8] S. Olyaee and A. M. Bahabady, Sens. Lett. **13** (2015) 1.

[9] A. K. Sana, K. Honzawa, Y.Amemiya, and S. Yokoyama, Jpn. J. of Appl. Phys. **55** (2016) 04EM11.

[10] M. Fukuyama, S. Yamatogi, H. Ding, M. Nishida, C. Kawamoto, Y. Amemiya, T. Ikeda, T. Noda, S. Kawamoto, K. Ono, A. Kuroda, and S. Yokoyama, Jpn. J. of Appl. Phys. **49** (2010) 04DL09.

[11] I. M. White and X. Fan, Opt. Express **16** (2008) 1020.

Chapter 3 Fabrication and measurements of photonic crystal resonators

3.1 Fabrication of Si photonic crystal resonator biosensor

The fabrication process of the PhC resonator sensor is shown in Fig. 3.1. (1) A 100-nm-thick oxide hard mask layer was first thermally grown on the SOI wafer surface as an intermediate layer of pattern transfer. (2) An electron beam (EB)-sensitive positive photoresist, ZEP520A, was spin-coated on the oxidized SOI wafer surface, and the photonic crystal hole pattern and waveguide were written using the Elionix ELS-G100 electron beam lithography system, which is of the point beam type. The pattern was then developed using xylene and isopropyl alcohol (IPA), the second lithography was carried out to form the PhC holes and cavity. (3) Then the sample with the oxide hard mask was dry-etched by reactive-ion etching (RIE) using CF_4 gas to transfer the pattern to the hard mask. (4) The patterns were the transferred to the device layer by inductively coupled plasma (ICP) etching of silicon using Cl_2 gas. After completion of the above process, wet etching was carried out using diluted HF solution to the remove the hard mask.

Steps of device fabrication

◆Thermal oxidation (100 nm)

◆Resist coating (ZEP520A)

◆Electron beam lithography (for waveguide)

◆Pattern developed using xylene and IPA

◆Electron beam lithography (for PhC and cavity)

◆Pattern developed using xylene and IPA

◆Reactive-ion etching of SiO_2 (using CF_4 gas)

◆Inductively coupled plasma etching of Si (using Cl_2 gas)

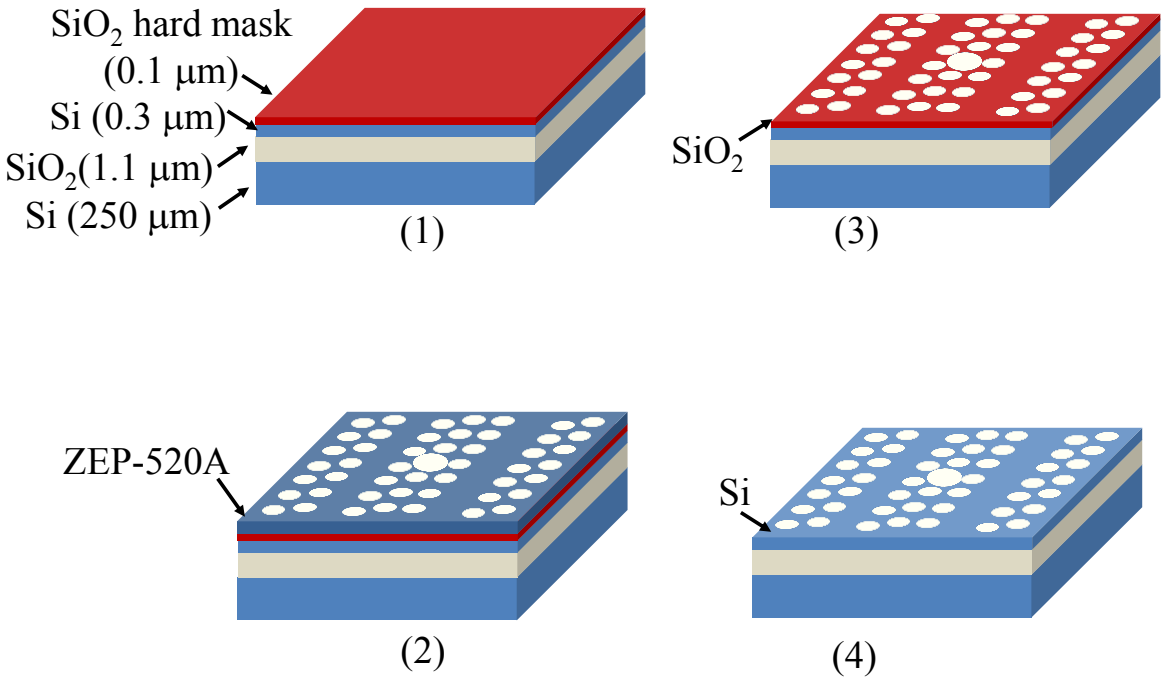

Fig. 3.1. Fabrication process of 2D photonic-crystal-based biosensor.[1)]

A comparison between two electron beam lithography machines (Hitachi HL-700, variable-shape beam type; Elionix ELS-G100, point beam type) is shown in Figs. 3.2(a) and 3.2(b), which show that the scattering of hole size in the case of using the ELS-G100 is much improved. In HL-700, the hole size was deformed owing its variable

shaped electron beam. On the other hand, in the case of using the ELS-G100 point beam system, the hole shape is improved similarly to the design.

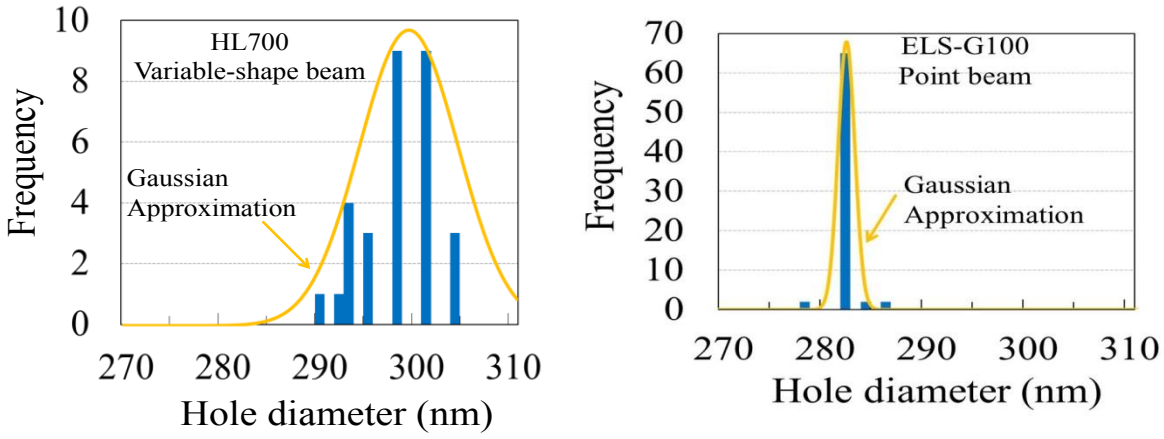

Fig. 3.2. Comparison of scattering of fine-tuned PhC hole fabrication between (a) HL-700 and (b) ELS-G100 electron beam lithography systems.[1)]

3.1.1 Reason for high *Q* by proposed device structures

In our proposed device structures, we got improved *Q* for both cavity, special shape cavity and double cavity with neighbor hole modulation that for point beam lithography systems (ELS-G100). The point beam lithography much improves the smoothness of the photonic crystal air holes and cavity region as well.

Scanning electron micrography (SEM) images of the fabricated cavity (400 nm), defect, and cavity (450 nm) are shown in Figs. 3.3(a)-3.3(c), respectively.

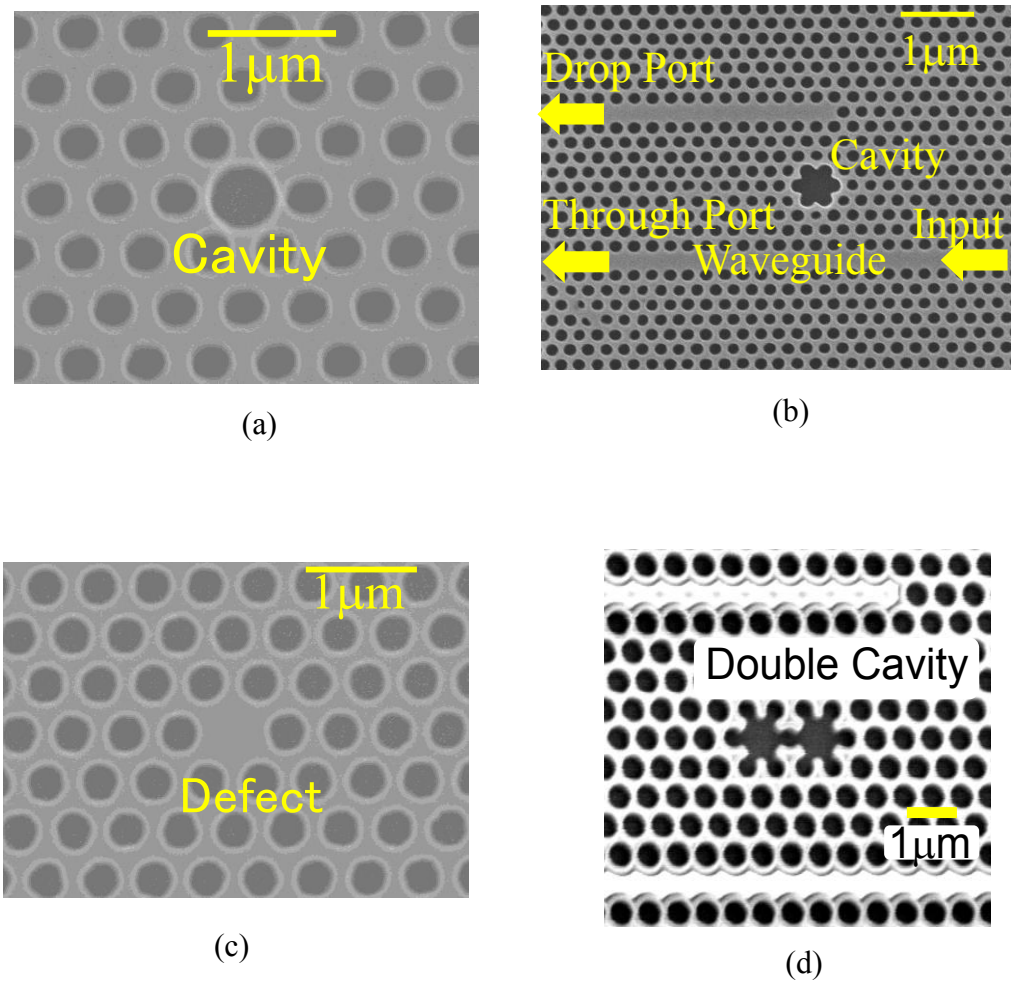

Fig. 3.3. SEM images of the fabricated devices: (a) cavity type (430 nm)[1] (b) cavity-type (450 nm)[1] where the center hole is connected to the surrounding holes, (c) defect-type[1] and (d) double cavity type (457 nm) where neighbor hole is modulated and connected with center cavity.[2]

3.2 Measurement system of Si photonic crystal resonator biosensor

3.2.1 Schematic of measurement systems

The schematic of optical measurements systems for the photonic crystal resonator biosensor is shown in Fig. 3.4. The light from the tunable laser source was coupled into the waveguide of the device by a lensed fiber, and the output was measured using an InGaAs photodetector.

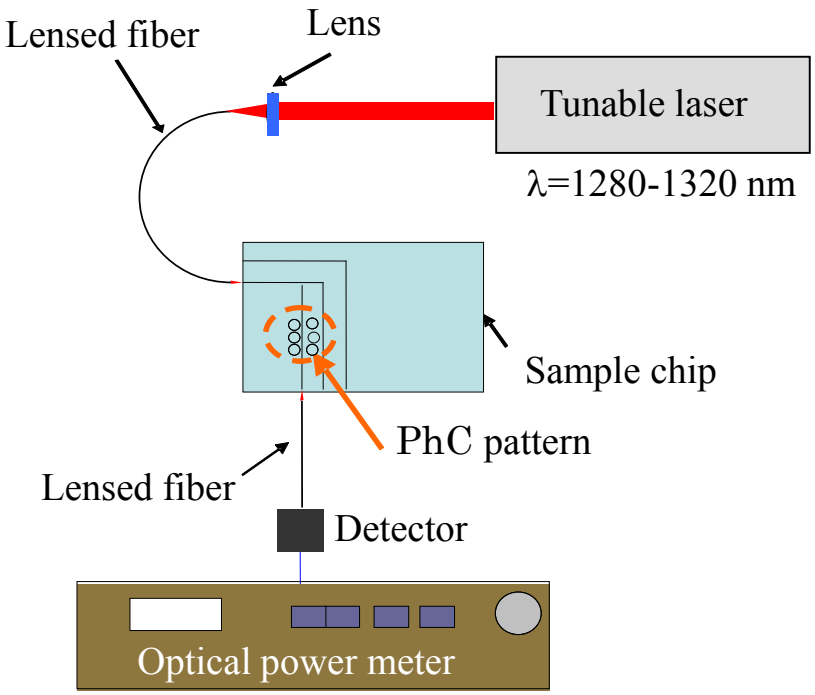

Fig. 3.4. Schematic of optical measurement sytems.[1)]

The photograph of the measurement system is shown in Fig. 3.5.

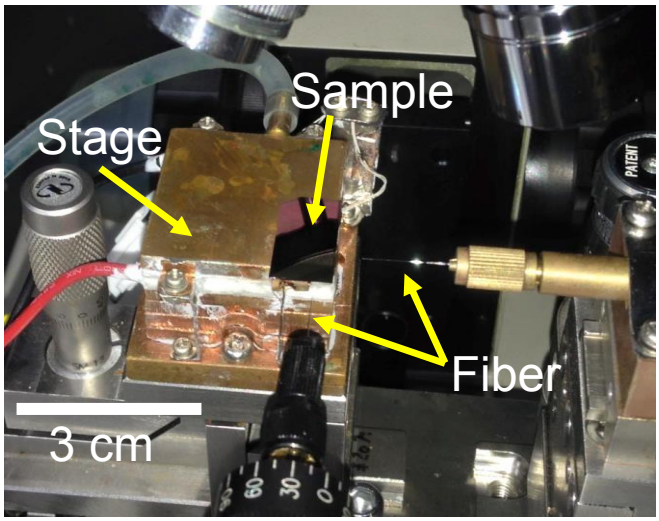

Fig. 3.5. Photograph of the optical measurements system.

References

[1] A. K. Sana, K. Honzawa, Y.Amemiya, and S. Yokoyama, Jpn. J. of Appl. Phys. **55** (2016) 04EM11.

[2] A. K. Sana, Y. Amemiya, and S. Yokoyama, "High sensitivity double-cavity silicon photonic crystal resonator for label free biosensor," Jpn. J. of Appl. Phys. **56** (2017) (Accepted for publication in 2017).

Chapter 4 Detection of device performance using sucrose solution

4.1 Sucrose solution preparation

The way to prepare sucrose solution is shown in Fig. 4.1. Deionized water (DI) of 900 μL and 0.1 gm sugar were mixed to make 10% of sucrose solution. After that, 0.1% sucrose solution was prepared by mixing with 900 μL DI water and 10 μL of 10% sucrose solution. Same way 0.2 % was prepared by mixing with 800 μL of DI water with 200 μL of 10% sucrose solution.

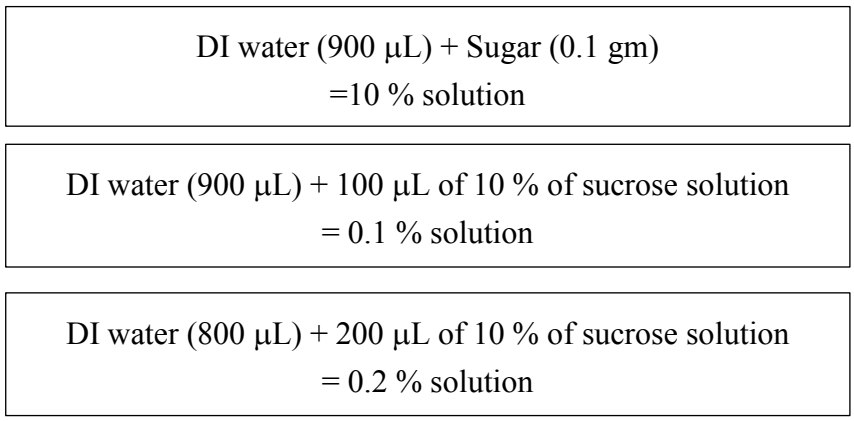

Fig. 4.1. Steps to prepare sucrose solution.

4.2 Measurement procedures

Firstly, for the sucrose detection, the device was cleaned by H_2SO_4+H_2O_2 solution after that we started measure sucrose solution at different concentration from lower to higher order. For the each concentration a 20 μL solutions were dropped to the sensor surface and wait for 10 min. After the waiting time we measured the resonant spectra for each concentration separately. The steps of experimental procedures are shown in Fig. 4.2.

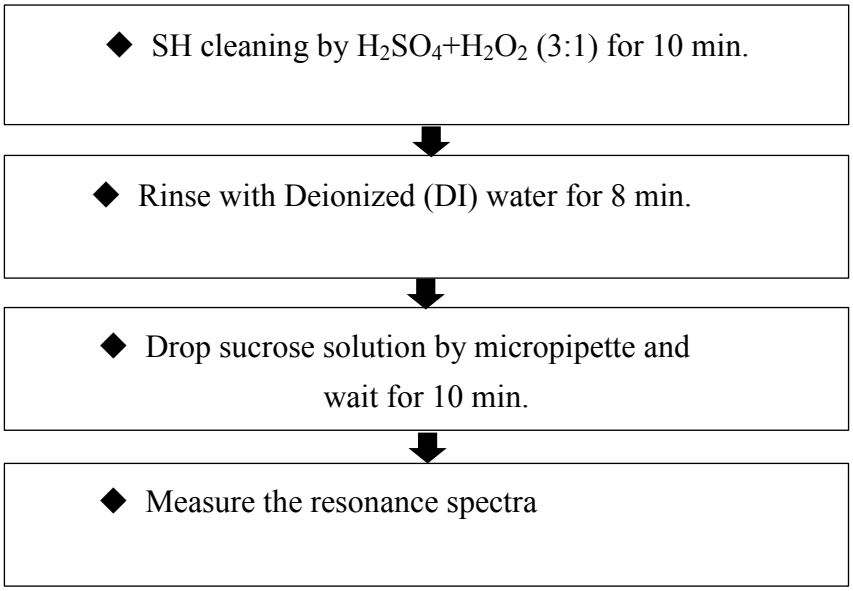

Fig. 4.2. Measurement steps of PhC resonator using sucrose solution.

After measuring each concentration, device should be cleaned at least four times by DI water.

4.3 Details about sucrose concentration and its corresponding refractive index

4.3.1 Measurement results

First, for the cavity-type resonator, the relationship between resonation wavelength and cavity size was simulated. The result is shown in Fig. 4.3 together with the experimental results. Cavity size has an important role in obtaining a resonance peak within the 1.3 μm range. To prevent water absorption loss, first of all, we consider that our optical power meter range lies between 1.28 and 1.32 μm. To obtain resonance wavelengths within this range, cavity size should also be considered in the design. The measured results are close to the simulated results.

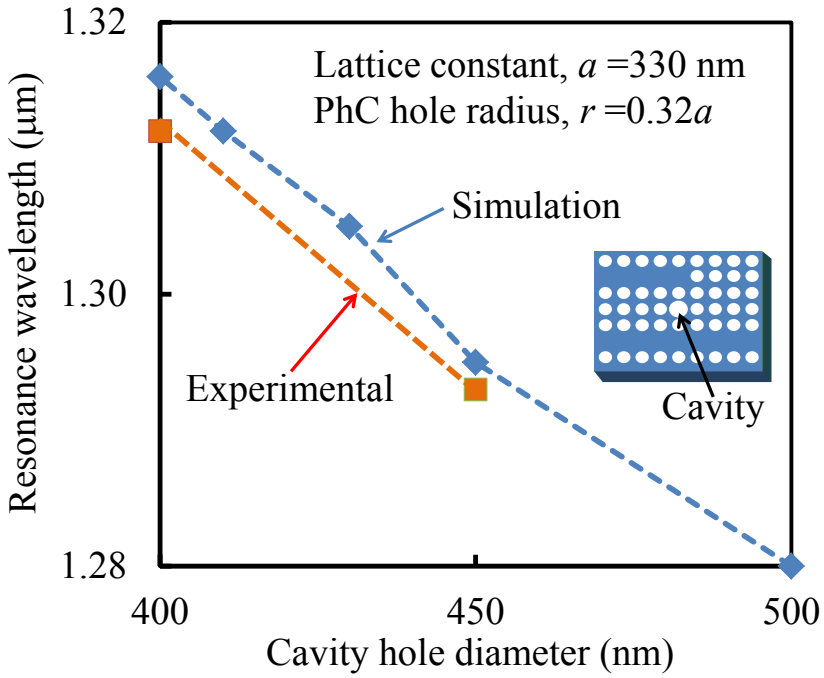

Fig. 4.3. Change in resonance wavelength with respect to cavity hole diameter.[1)]

Figure 4.4 shows the simulated results of the cavity diameter dependence of the resonance wavelength shift at 0.1% sucrose concentration. The simulation results for the defect-type resonator (one hole missing) and the measured results for the cavity-type resonator with an abnormal shape of the cavity (will be discussed later) are also shown. The resonance wavelength shift becomes large with increasing cavity size. The

phenomenon clearly shows why a large cavity offers a larger wavelength shift than other structures. The large cavity is filled up with the highest amount of target molecules, as a result the confined photons interact markedly with the molecules; finally, the wavelength shift becomes large.

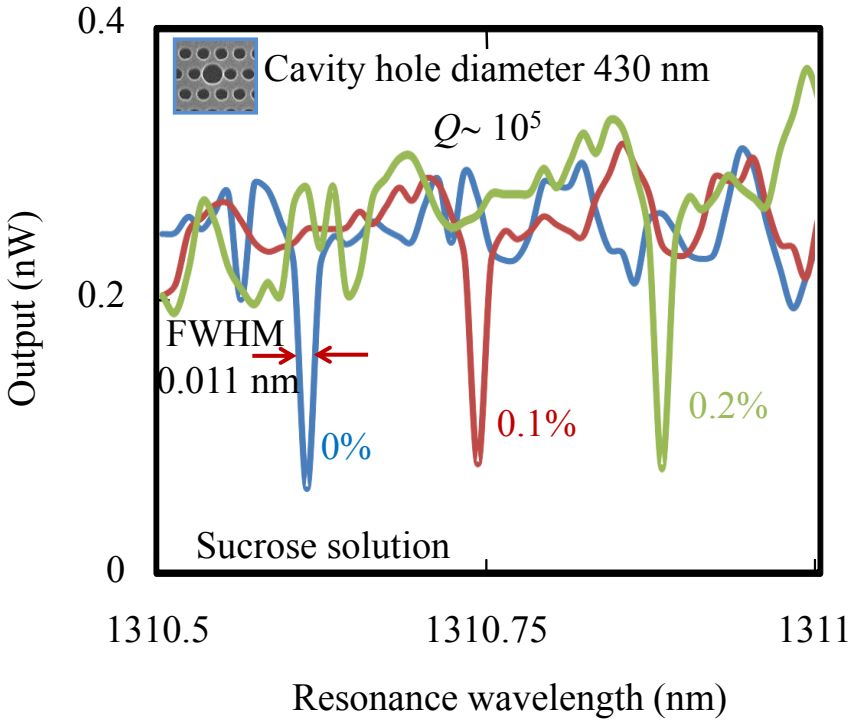

Fig. 4.4. Resonance wavelength shift ($\Delta\lambda$)/sucrose concentration with respect to cavity hole diameter.[1)]

The measured results for the sucrose solution are shown in Figs. 4.5 and 4.6, respectively, for the normal cavity hole (diameter of 430 nm) and abnormal cavity hole (accidentally a too large hole was formed and it is connected to the surrounding holes). We measured the output of the through port because the output of the drop port was weak for some reason (for example, caused by the defects in the waveguide connecting to the drop port). We observed clear dips due to the resonation. It is clearly observed that the resonance wavelength has shifted with sucrose concentration change.

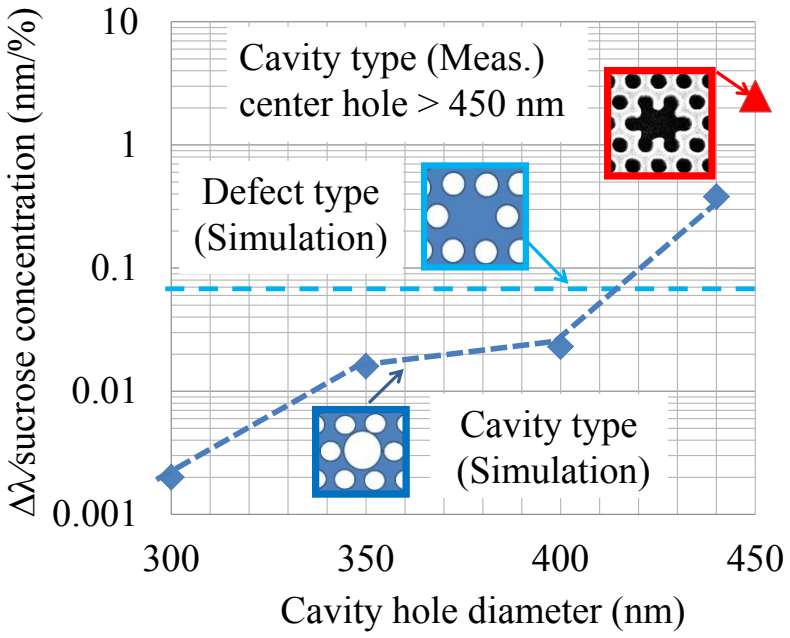

Fig. 4.5. Measured results of fabricated device with cavity hole diameter 430 nm.[1)]

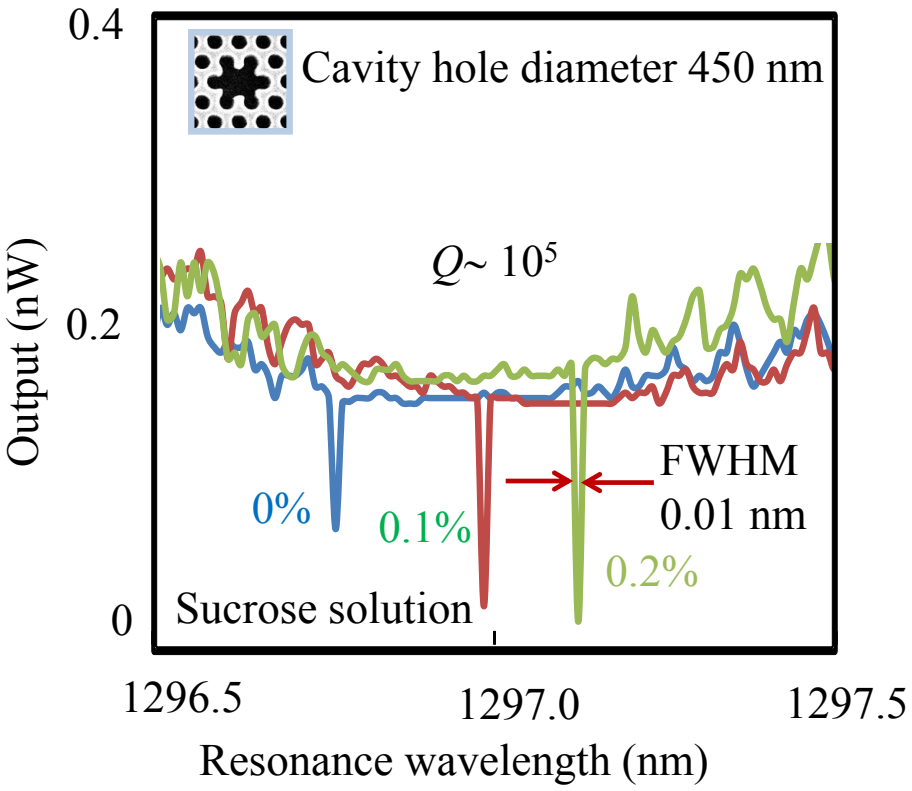

Fig. 4.6. Measured results of fabricated device with cavity hole diameter 450 nm.[1)]

In the double nanocavity resonator type device the neighbor hole radius are varied and we got highest Q-factor at certain radius. The experimental result of double nanocavity type resonator at various sucrose concentrations is shown in Fig. 4.7. The observed resonance peaks have very small full width at half maximum (FWMH) of 6.5 to 6.9 pm and the Q-factor about (1.93 ~ 2.02) $\times 10^5$ is derived from the various FWHM.

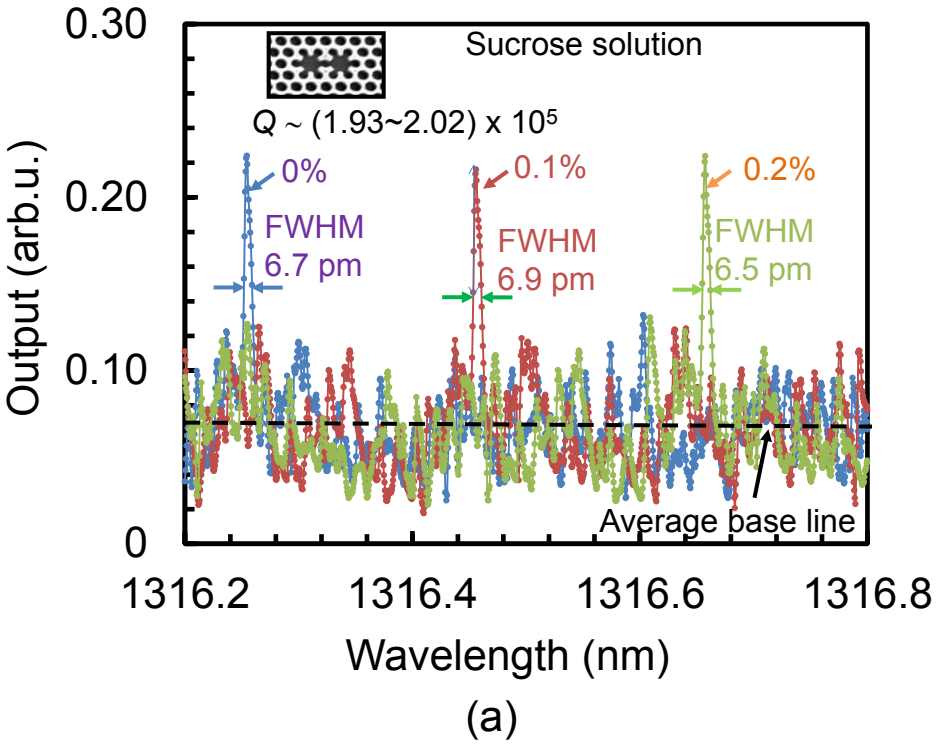

Fig. 4.7. Measured results double nanocavity resonator.[2)]

The simulation result of Q-factor versus neighbor hole radius is shown in Fig. 4.8(a) together with the experimental data. The results show that the Q value becomes high at certain neighbor holes radius.

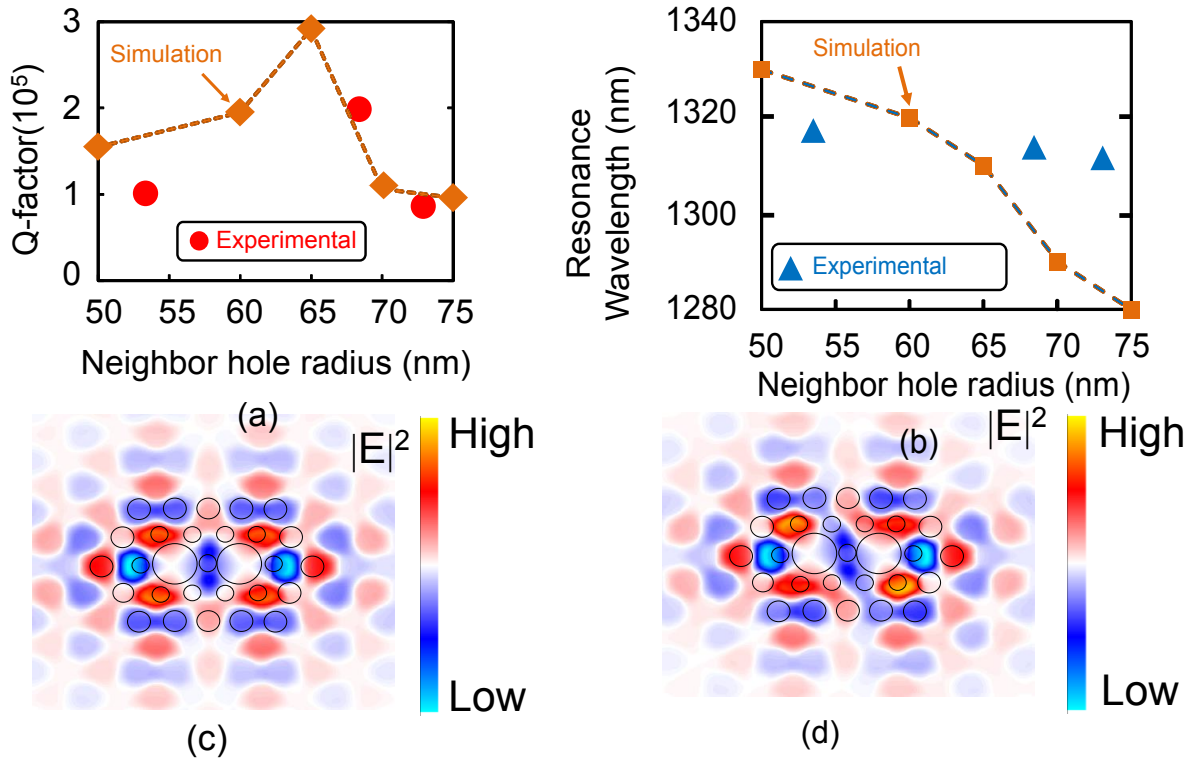

Fig. 4.8. (a) Neighbor hole radius versus Q value, (b) neighbor hole radius versus resonaonce wavelength, (c) electric field distribution at neighbor hole 65 nm and (d) electric field distribution at neighbor hole 70 nm.[2)]

In Fig. 4.8(b) the simulated and experimentally observed resonance wavelengths are plotted. The deviation between simulation and experiment is larger at the larger neighbor hole sizes. This trend may be explained by the proximity effect during the electron beam lithography process

Figure 4.8(c) and Fig. 4.8(d) it is recognized that the light intensity is strong at the neighbor holes, then its size strongly affects the resonance characteristics, but the detailed physical mechanism of the enhancement of Q-factor is not clear at this stage.

4.4 Linearity check with resonant wavelength shift by the sucrose concentration

As we measured our device performances using sucrose solution and we took attention that resonance wavelength shift should be linear with sucrose concentration. In Fig. 4.9, for the abnormal cavity shape, the wavelength shift does not linearly change with increasing sucrose concentration. The possible reason is that air bubbles are adsorbed on the sidewall of the cavity. The results of two different cavity hole size structures show that, the cavity with a large hole induces a greater resonance wavelength shift than that with a small one. In our measured results, the abnormal cavity shape (designed cavity size is 450 nm) has about 1.7 times larger wavelength shift at 0.1% sucrose concentration than the small cavity (430 nm). We confirmed a large 2.3 times wavelength shift of the large-cavity- type structure compared with that of the defect-type at 0.1% sucrose concentration.

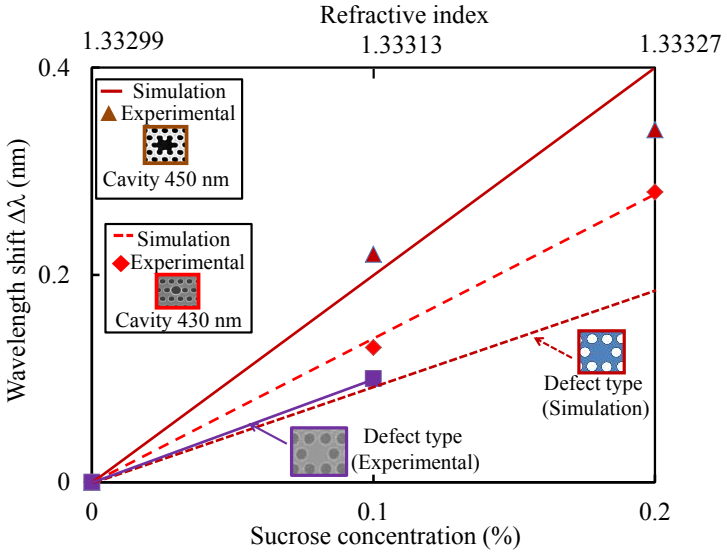

Fig. 4.9. Sucrose concentration vs resonance wavelength shift.[1)]

The sucrose concentration versus resonance wavelength shift for double nanocavity resonator is shown in Fig. 4.10.

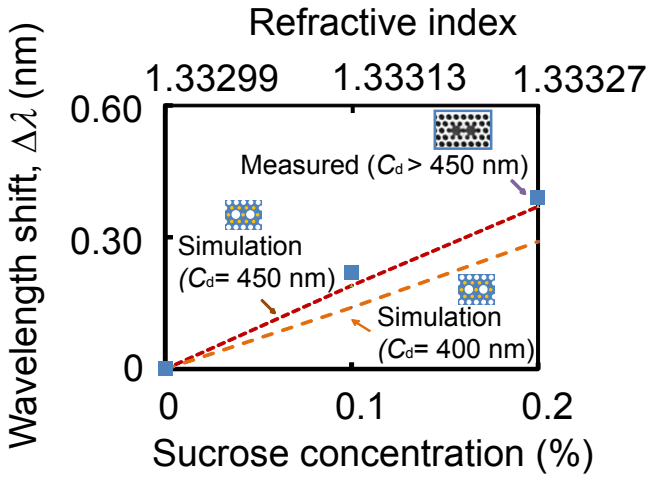

Fig. 4.10. Sucrose concentration vs resonance wavelength shift.[2)]

References

[1] A. K. Sana, K. Honzawa, Y.Amemiya, and S. Yokoyama, Jpn. J. of Appl. Phys. **55** (2016) 04EM11.

[2] A. K. Sana, Y. Amemiya, and S. Yokoyama, "High sensitivity double-cavity silicon photonic crystal resonator for label free biosensor," Jpn. J. of Appl. Phys. **56** (2017) (Accepted for publication in 2017).

Chapter 5 Detection of antigen-antibody reaction

5.1 Details of Si-tag, protein-G, antibody (IgG2a) and prostate specific antigen

Rapid and early diagnosis is demanded for the aging society[1)] to providing better quality of life as well as to minimize the healthcare expenses.[2)] Conventional biosensors based on enzyme-linked immunosorbent assays (ELISA)[3, 4)] requires a number of steps, including the use of a labeling target molecules to get a detectable signal. A lot of study has been devoted to the developed the fast, accurate, and label-free biosensors to enhance medical diagnostics, biomolecules, and organic chemical detection.[5-9)] Photonic crystal[10-12)] based micro/nano cavities getting lots of research interest for medical diagnosis purpose due to their strong light confinement nature, high quality factors (Q) and small modal volumes. By introducing a defect in the photonic crystal periodic structure, the light of certain resonance frequency are possible to confine into the defect or cavity region. When the local refractive index of the sensor surface is changed then resonant wavelength shifts. These shifts are the main key parameter to measure the device sensitivity

The uniqueness of this work is the silicon binding protein that binds with SiO_2 and Si surface and immobilizes the biomolecules on the PhC cavity surface. The things that we used are the protein G (Pro-G) which makes strong bonds with many kinds of mammalian antibodies. The antigen-antibody reaction procedure is shown in Fig. 5.1. In Fig. 5.1(a), the receptors are randomly oriented. In this method antigen-antibody immobilization on sensor surface is difficult. In Fig 5.1(b), Si-tag were used to immobilize the antigen-antibody on the sensors surface and role of Pro-G is shown in Fig. 5.1(c). The PhC nano-cavity resonator is immersed in the solution containing the Si-tagged Pro-G, which immobilizes the bioreceptors on the Si/SiO_2 surface, and then immersed in the antibody (mouse antibody subtype IgG2a) solution. After that, the resonator is immersed by the target antigen of PSA. The resonance spectra have been measured at each step.

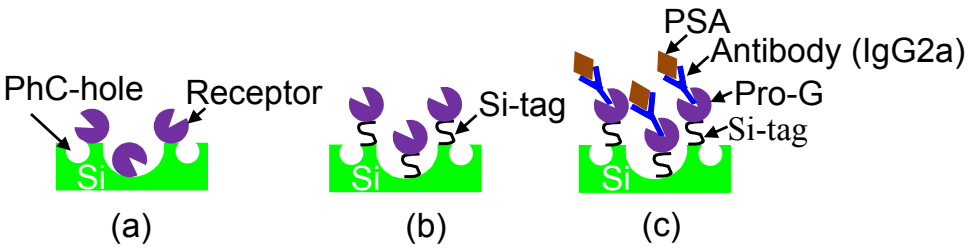

Fig. 5.1. Role of Si-tag (a) without Si-tag (b) with Si-tag and (c) role of Protein G.[13, 14)]

5.2 Measurement procedures

The measuring steps of PSA are explained in Fig. 5.2. First, the Si-tagged protein G was poured on the surface sensor, and then the resonance spectrum was measured. Secondly, the anti-PSA or antibody (named as IgG2a) was added to the solution, the resonance wavelength was shifted. Next, PSA antigens were added to the solution, and measured the spectral shift of resonance peak. Buffer solution (Tris-HCl) was used to remove the unreacted biomolecules from the sensor surface. The resonance spectra for various concentrations were measured from lower to higher concentration.

◆SH cleaning by H_2SO_4+H_2O_2 (3:1) for 10 min

◆Rinse with Deionized (DI) water for 8 min

◆Sensor surface clean by Buffer solution (Tris-HCl) and wait for 10 min

(1)
- ◆Drop 20 μL of Si-tag + Pro-G and wait for 10 min
- ◆Clean by Tris-HCl
- ◆Drop 20 μL of IgG2a (Antibody) and wait for 10 min
- ◆Clean by Tris-HCl
- ◆Measurements

(2)
- ◆Drop 20 μL of PSA(antigen) and wait for 10 min
- ◆Clean by Tris-HCl
- ◆Measurements

Steps (2) should be repeated from lower concentration to higher concentration.

Fig. 5.2. Measurement steps of PhC resonator using antigen-antibody reaction.

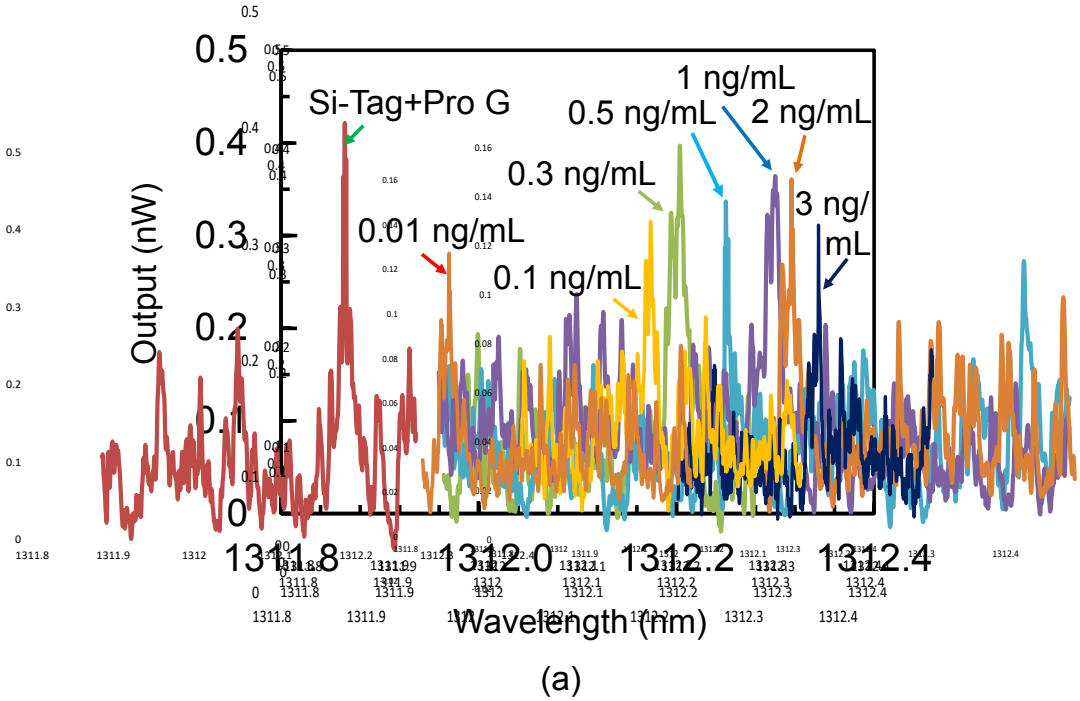

Fig. 5.3. Experimental results of different PSA conentration.

5.3 Resonance characteristics versus PSA concentrations

Finally, we measured prostate specific antigen (PSA) biomarker. In many cases, concentration of PSA of 4 ng/mL in the blood is considered the prostate cancer positive. The sensitivity of the biosensor is required to detect less than 1 ng/mL. The experimental procedure is explained in Fig. 5.2. First, the Si-tagged protein G was poured on the surface sensor, and then the resonance spectrum was measured. Secondly, the anti-PSA or antibody (named as IgG2a) was added to the solution, the resonance wavelength was shifted. Next, PSA antigens were added to the solution, and measured the spectral shift of resonance peak. Figure 5.4 shows the resonance spectra of Si-tag+proG and several of PSA concentrations and it also shows that at each concentration resonance spectra has shifted and at higher concentration the shift is going to be saturated.

5.4 Measurements results fitting with Langmuir's curve

In Fig. 5.3 the resonance wavelength shift (Δλ) is plotted as a function of the concentration of the PSA solution. The result fits to the following Langmuir equation,[15)]

$$\Delta\lambda = \frac{\Delta\lambda_{\max} CK}{1+CK}, \tag{5.1}$$

where $\Delta\lambda_{\max}$ is the maximum resonance wavelength shift, C is the concentration of PSA biomarkers and K indicates the equilibrium constant of adsorption-desorption reaction. The best fitting is shown in Fig. 5.4 by adjusting the K values.

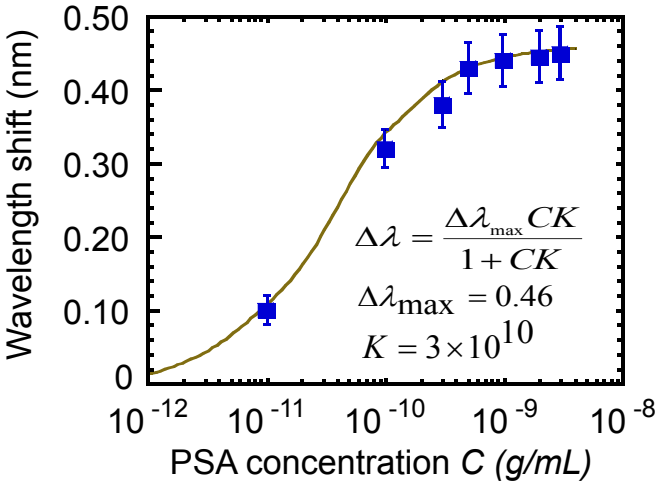

(b)

Fig. 5.4. Langmuir's fitting with experimental results.

5.5 How could linearity improvement is possible in saturated region at higher concentration of biomaterials

As in Fig. 4.9, the resonance wavelength shift of various device structures are shown. Both cavity and special shape cavity has larger wavelength shift and these two structures will saturate quickly at higher concentration. However in the defect type structures, the shift is smaller than other structures. As for the small shift, the linearity at higher concentration may be possible by using defect type device.

References

[1] G.-J. Zhang, Z. H. Luo, M. J. Huang, J. J. Ang, T. G. Kang, and H. Ji, Bios. Bioele. **28** (2011) 459.

[2] T. Taniguchi, A. Hirowatari, T. Ikeda, M. Fukuyama, Y. Amemiya, A. Kuroda, and S. Yokoyama, Opt. Comm. **365** (2016) 16.

[3] C. Liu, F. Wang, T. Sun, Q. Liu, H. Mu, and K. P. Chu, J. Nanophot. **9** (2015). 093050(1-10).

[4] R. S.Yalow and S. A. Berson, Clin. Invest. **39** (1960) 1157.

[5] E. K. Akowuah, T. Gorman, H. Ademgil, S. Haxha, G. K. Robinson, and V. Oliver, IEEE J. of Quan. Elect. **48** (2012) 1403.

[6] J. A. Kim, T. Hwang, S. R. Dugasani, R. Amin, A. Kulkarni, S. H. Park, and T. Kim, Sens. Actu. B **187** (2013) 426.

[7] J. Homola, Anal. Bioanal. Chem. **377** (2003) 528.

[8] R. Otupiri, E. K. Akowuah, S. Haxha, H. Ademgil, F. Abdelmalek, and A. Aggoun, IEEE Phot. J. **6** (2014) 6801711.

[9] G. J. Ortega-Medoza, A. P. Vivanco, C. T. Quitl, P. Z. Morán, V. Hernández, and F. Chávez, Sens. **14** (2014) 18701.

[10] E. Chow, A. Grot, L. W. Mirkarimi, M. Sigalas, and G. Girolami, Opt. Lett. **29** (2004) 1093.

[11] M. Lee and P. M. Fauchet, Opt. Express **15** (2007) 4530.

[12] S. Hachuda, K. Watanabe, D. Takahashi, and T. Baba, Opt. Express. **24** (2016) 12886.

[13] T. Ikeda, Y. Hata, K. Ninomiya, Y. Ikura, K. Takeguchi, S. Aoyagi, R. Hirota, and A. Kuroda, Anal. Biochem. **385** (2009) 132.

[14] K. Taniguchi, K. Nomura, Y. Hata, T. Nishimura, Y. Asami, and A. Kuroda, Biotechnol. Bioeng. **96** (2007) 1023.

[15] I. Langmuir, J. Am. Chem. Soc. **38** (1916) 2221.

Chapter 6 Temperature independent device for the biomaterial sensing

6.1 Temperature effects on resonance wavelength shift

The refractive index (RI) of silicon greatly changes with temperature change.[1,2] The effective refractive index of the sensor surface (Si ring resonator, PhC cavity resonator or any other RI based sensor) changes due to the adsorption target material. Then it becomes difficult to measure target material induced resonance wavelength shift precisely because of the thermal fluctuation changes the silicon refractive index as well as takes part on the resonance wavelength shift. Controlling the thermal effects is important to detect the biomaterials perfectly as the effective refractive changes with temperature change. The change in biomolecules concentration induces the change in local refractive index as a result resonant wavelength shift occurs. However the silicon itself has large thermo-optic coefficient[3] ($dn/dT=1.8\times10^{-4}$/°C, where n is refractive index and T is temperature). Furthermore deformation of the device mechanical shape due to temperature change induces the resonance wavelength. Due to large thermo-optic coefficient of Si, active thermal controller is needed to detect the biomolecules precisely. However, for the low cost applications, active thermal control is often not feasible. Several thermal effect compensating devices so that they can be used without any thermal controller, have previously been shown[4-19] by designing the specific device structure that compensate thermal effects. As the temperature changes, the device mechanical deformations happen together with the refractive index change of Si.

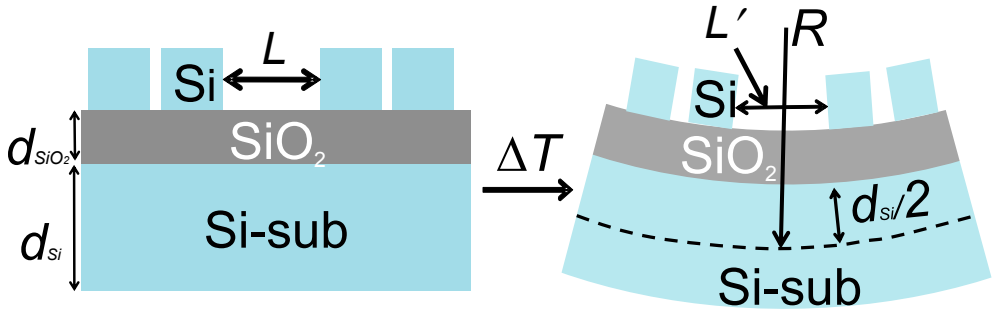

Fig. 6.1. Curvature shape of thin Si layer due to mechanical deformation by temperature change.

6.2 Numerical analysis and simulation

Resonance wavelength shift of Si resonators by thermal change is given by the following equation,

$$\Delta\lambda_{res} = \frac{\Delta n_{eff}}{n_{eff}}\lambda_{res} + \frac{\Delta L}{L}\lambda_{res} \ , \tag{6.1}$$

where λ_{res}, n_{eff} and L are the resonance wavelength, effective refractive index and size of the resonator respectively. $\Delta\lambda_{res}$, Δn_{eff} and ΔL are the change in these values due to the temperature change. The right hand first term indicates the effective refractive index (Si) effect and latter term indicates the thermal deformation effect. This equation is easily derived from the equation of $\lambda_{res} = n_{eff}L/m$, where m denotes the integer. As the temperature increases, Si and SiO_2 thermally expand with different thermal expansion coefficients and the SOI wafer has a curvature shape as shown in Fig. 6.1. The radius of the curvature of the SOI substrate is given by the following equation,[22)]

$$\frac{1}{R} = \frac{6(\alpha_1 - \alpha_2)\Delta T(1+p)^2}{h\left[3(1+p)^2 + (1+pq)(p^2 + \frac{1}{pq})\right]}, \tag{6.2}$$

where h, α_1 *and* α_2 are the total thickness and thermal expansion coefficient of Si and SiO_2, $p=d_{SiO2}/d_{Si}$ (where d_{SiO2} and d_{Si} are the thickness of SiO_2 and Si, respectively), $q = Y_{SiO2}/Y_{Si}$ (where Y_{SiO2} and Y_{Si} are Young's modulus of SiO_2 and Si) and ΔT is the temperature change. The change in resonator size is expressed as follows

$$\Delta L \approx \frac{dL}{2R}, \tag{6.3}$$

where d is the thickness of SOI substrate. Here, $d=d_{Si}+d_{SiO2}$ and $d_{Si} >> d_{SiO2}$ is assumed.

In the differential silicon ring resonator, one ring is considered as detection ring, on which a biomaterial is adsorbed and other is considered as reference ring, which is not exposed to the biomaterial. The phase of one of the outputs is changed by π and merged again. When a biomaterial is not adsorbed on the detection ring, the differential output is zero because these two resonance curves completely overlap. When a biomaterial is adsorbed on the detection ring, its resonance curve shifts and an output signal appears. Here, we discuss the output spectrum of the differential ring resonator sensor. First, for the single-ring resonator the transmission spectrum T_S is given by the following equations[24, 25)]

$$T_s = \frac{\sin K[1 - X\cos\phi(\lambda) + i\sin\phi(\lambda)]}{1 + X^2 - 2X\cos\phi(\lambda)}, \tag{6.4}$$

$$X = \cos^2 K \exp(-\frac{\alpha L}{2}), \tag{6.5}$$

$$\phi(\lambda) = \frac{2\pi n_{eff} L}{\lambda}, \tag{6.6}$$

where sin K is the coupling coefficient, α is the attenuation constant of the waveguide, L is the peripheral length of the resonator, and n_{eff} is the effective refractive index of Si waveguide. The transmission spectrum of the differential Si ring resonator sensor T_{DS} is given by[20)]

$$T_{DS} = \left|T_S + e^{i\theta}T_S\right|^2 + (2 + 2\cos\theta)|T_S|^2, \tag{6.7}$$

where θ is the phase difference between the detection ring and reference ring and usually π.

The temperature dependence is calculated by using following equations

$$\theta = \frac{2\pi n_{eff}\,\Delta l}{\lambda}, \tag{6.8}$$

$$n_{eff} = n_{23} + \beta\,(T - 23) \tag{6.9}$$

where Δl is the length of the phase shifter, T (℃) is the temperature, n_{23} is the effective refractive index at 23 °C , and β is thermal coefficient of core and various clad layer and at the above temperature . n_{23} and β are obtained by using the following equation.

$$n_{eff}\left(\frac{dn_{eff}}{dT}\right) = \left(n_1 \frac{dn_1}{dT}\Gamma_1\right)_{core} + \left(n_2 \frac{dn_2}{dT}\Gamma_2\right)_{topclad} + \left(n_3 \frac{dn_3}{dT}\Gamma_3\right)_{bottomclad}, \tag{6.10}$$

where n_1, n_2, n_3 are refractive index of core, top clad and bottom clad respectively. the thermal coefficient of core, top clad and bottom clad are dn_1/dT, dn_2/dT and dn_3/dT respectively. Γ_1 , Γ_2 and Γ_3 are the electric field confinement factor of core, top clad and bottom clad respectively, which were obtained from the simulation using Rsoft photonic CAD suite (Synopsys Inc.). The equation (6.9) is obtained by optical simulator. Using the values of the bulk materials are obtained from Refs. 26 for oil , and 27 for silicon, SiO_2, resist and air. The actual numerical values of coefficient $\beta = 1.16 \times 10^{-4}$/ °C and for SiO_2 and $\beta = 1.14 \times 10^{-6}$/ °C for water, $\beta = 1.09 \times 10^{-4}$/ °C for air, $\beta = 1.15 \times 10^{-4}$/ °C for oil, and $\beta = 1.15 \times 10^{-4}$/ °C for resist respectively.

In the differential mode, wide bandwidth input light can be used and the output is the integral of the light intensity within the input light bandwidth or the maximum peak height.

Figure 6.2 shows the maximum differential output versus $\Delta n_{\text{eff}}/n_{\text{eff}}$ or $\Delta L/L$ which is difference in the effective refractive index or circumferential length of Si waveguide between the detection and reference resonators divided by the original ones respectively. It is found that there is a linear region in the output versus $\Delta n_{\text{eff}}/n_{\text{eff}}$ or $\Delta L/L$ curve. The Δn_{eff} or ΔL induces $\Delta\lambda_{\text{res}}$ which is difference in the resonance wavelength between the two rings. In the linear region even though the resonance wavelengths of both resonators are slightly different, the sensitivity which defined as output/Δn_{eff} or output/$\Delta\lambda_{\text{res}}$, becomes constant when the operation point is in the linear region.[20)]

Figures 6.3 and 6.4 shows the calculated temperature change versus maximum output change for various cladding layers (e.g. air, water, resist, oil, and SiO_2).

To simulate the temperature dependence of photonic crystal resonator sensor we used equation (6.1)-(6.3) and equation (6.10). The length L for photonic crystal resonator is considered the maximum electric field distributed area. The field is distributed in the Si, resonator inside as well as in the SiO_2 layer. The confinement factor Γ_1, Γ_2 and Γ_3 are for the inside of the resonator area, Si and SiO_2 respectively. The simulated electric field distribution using the Rsoft photonic CAD suite is 58%, 22% and 20% of inside of the resonator region, Si and SiO_2 respectively.

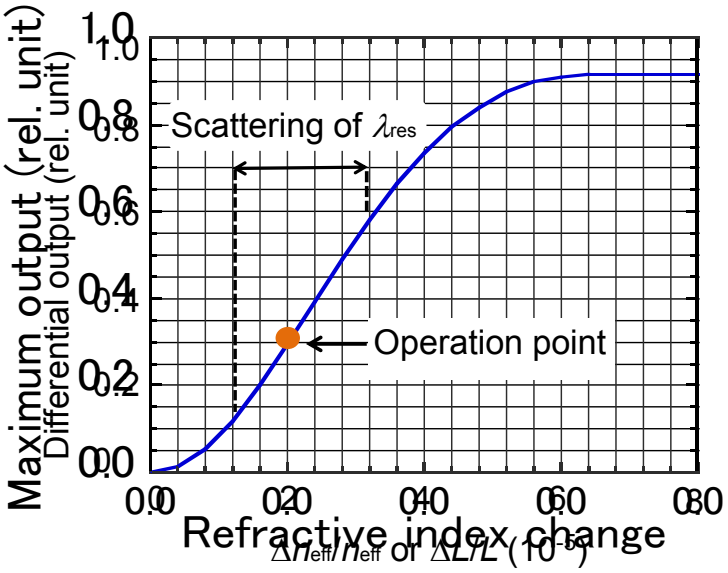

(a)

Fig. 6.2. Simulation results of refractive index versus maximum output change.

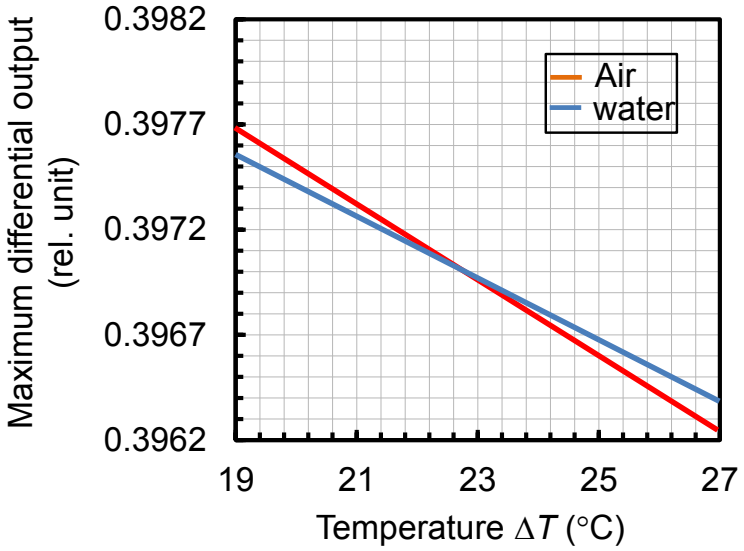

(b)

Fig. 6.3. Simulation results of temperature change versus maximum differential output variation at various cladding layer such as air and water.

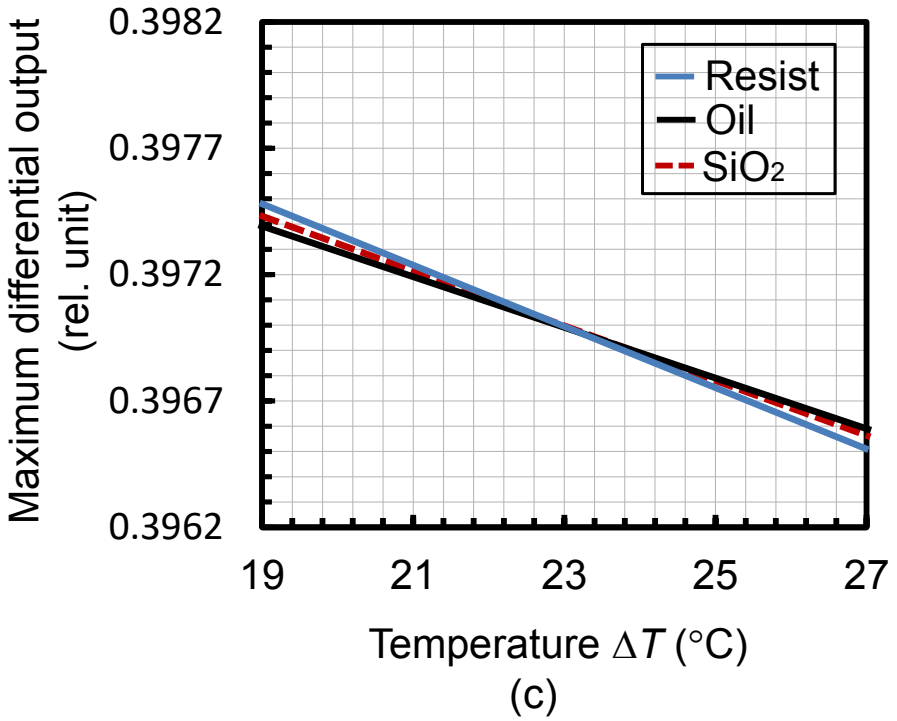

(c)

Fig. 6.4. Simulation results of temperature change versus maximum differential output variation at various cladding layer such as resist, oil and SiO_2.

6.3 Schematic of device structures of differential Si ring resonators

In this work, the resonance wavelength shifts of Si ring and photonic crystal resonators on silicon-on-insulator (SOI) substrate were investigated. In order to solve the temperature instability we proposed a differential operation of two resonators,[20] where a π phase shifter is installed in one of the two outputs before merging. In this case the integral intensity of the differential output becomes temperature independent because the resonance wavelengths of both two resonators shift in parallel. The schematic structure of the differential Si ring resonator and photonic crystal (PhC) based cavity type resonators[21] are shown in Figs. 6.5(a) and 6.5(b) respectively.

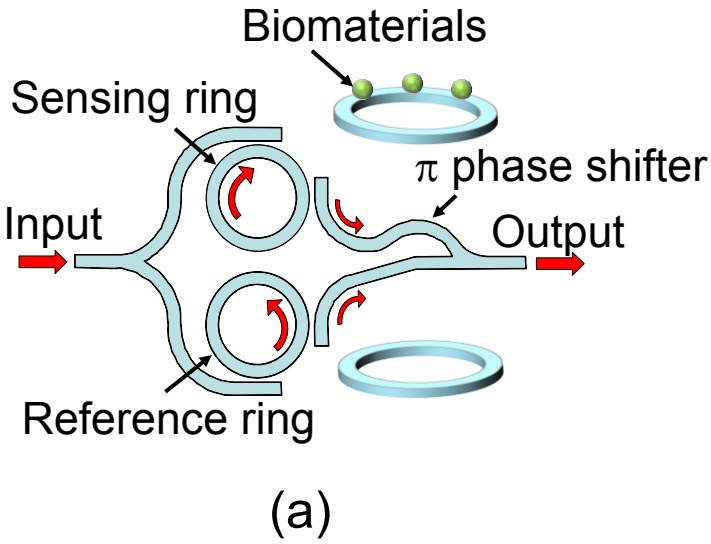

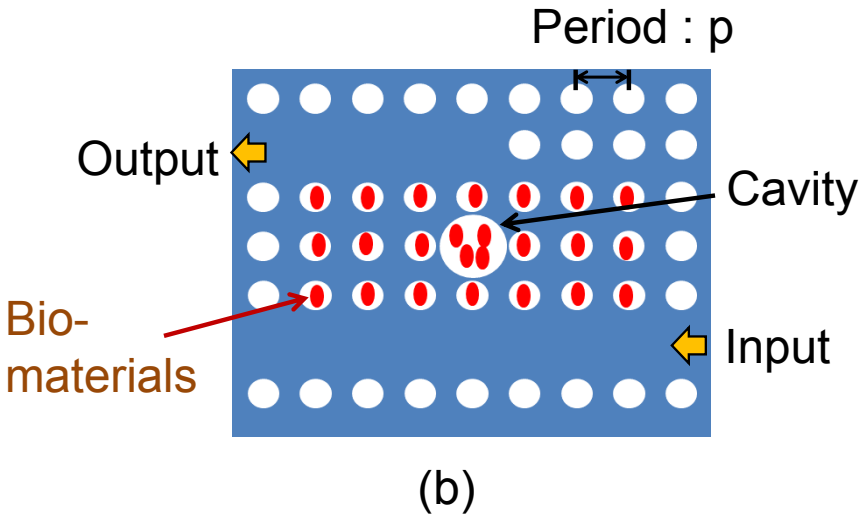

Fig. 6.5. (a) Schematic of differential Si ring resonator biosensor and (b) photonic crystal cavity resonator.

6.4 Measured results

6.4.1 Mechanism of thermal change of λ_{res} of Si ring and PhC resonators

The temperature dependence of the differential Si ring and PhC cavity resonators are shown in Figs. 6.6 and 6.7 respectively. In Fig. 6.8(a) the measured results for the differential Si ring resonators at different temperature are shown together with the simulation results obtained by the method described in Sect. 6.2. It is found that the measured data well fits to the simulation result and it is clear that Si refractive index change effect is dominating. The mechanical deformation effect is negligible ($\Delta\lambda_{res}/\Delta T$~ -10^{-4} nm/°C). The result for the PhC resonator is also shown in Fig. 6.8(b), and the same conclusion as for the ring resonator is derived. For the both type of devices, we simulated by using equation (6.10) and considered core, top clad and bottom clad each layer's effect individually. The calculated field distribution in the core (Si), top clad (air) and bottom (SiO_2) clad are 80%, 8% and 12% respectively.

6.4.2 Thermal stability of differential Si ring resonator sensor

In Fig. 6.9 the maximum of differential output change for ΔT =4℃ from 25 °C to 29 °C for the Si ring resonators with different top cladding layers are plotted. In the differential detection, only the maximum differential output is counted, which corresponds to the difference between the resonance wavelength shifts of two rings. And the spectral shift of the differential output is not counted. Theoretically, the maximum differential output change for ΔT=4℃ is calculated at three different top cladding layer conditions, the simulated change for resist, air and oil are 0.012%, 0.02% and 0.01% respectively indicated by ⌶. The measured results is also shown in Fig. 10, where the changes in maximum differential outputs for the differential Si ring resonators with different top cladding layers for ΔT =4℃ are plotted. Measured scatter error for multiple measurements in air clad is represented by ⌶ (reproducibility at the same condition). And measured data deviation with the temperature changes (25 °C to 29 °C) is expressed by ▮. The theoretical calculation suggests that temperature independence of the differential operation is right.

In our research we targeted to detect prostate specific antigen (PSA) of 1 ng/mL as practical sensitivity. We used various concentrations of sucrose solutions and the conversion of equivalent refractive index was done by the help of Ref. 28 and 29. The sucrose solution at 10^{-2} % concertation corresponds to 1 ng/mL of PSA. The change in effective refractive index for 1 ng/mL PSA is equivalent to $\Delta n_{\text{eff}} \approx 1.7\times10^{-5}$ (Ref. 20) and $\Delta n_{\text{eff}}/n_{\text{eff}}$ is the 6.5×10^{-6}, which corresponds to the differential output of 0.186 from Fig. 6.2. This is on the linear region of this graph. As the differential output is in the linear region, output/$\Delta\lambda_{\text{res}}$ could be constant even though the temperature increases.

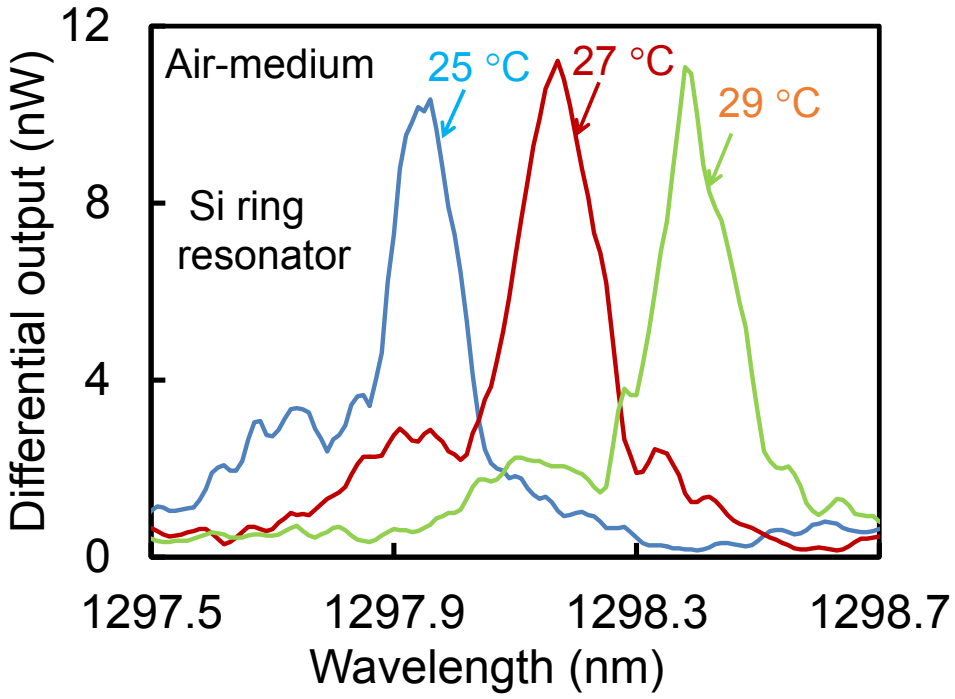

Fig. 6.6. Measurement results of differential Si ring resonator at different temperatures. Top cladding layer is air.

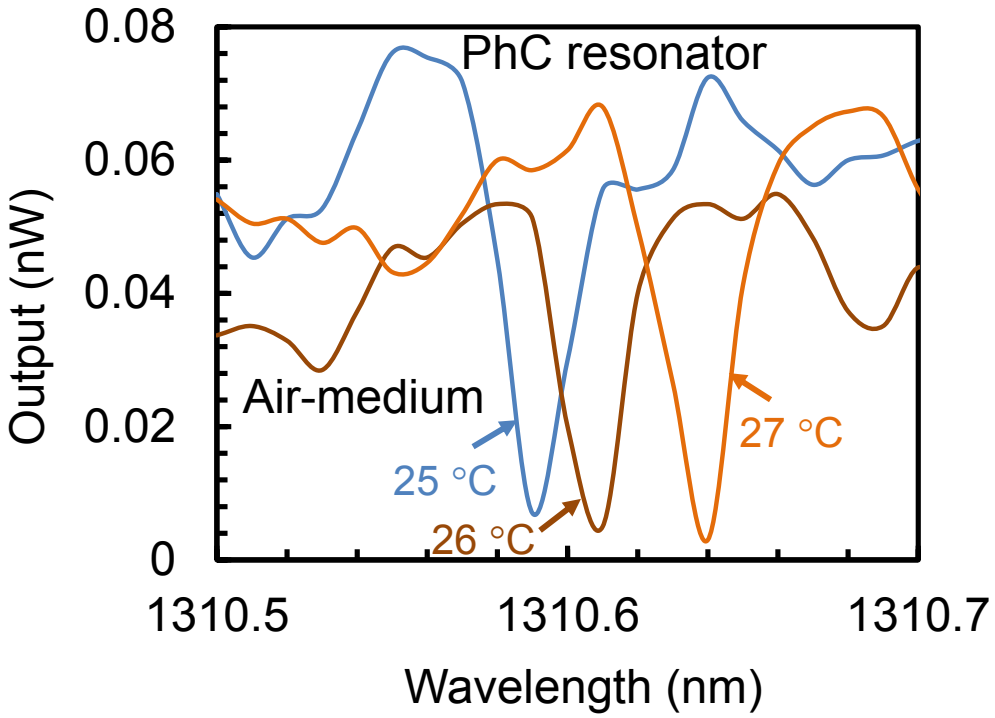

Fig. 6.7. Resonation spectra of PhC cavity resonator at various temperatures.

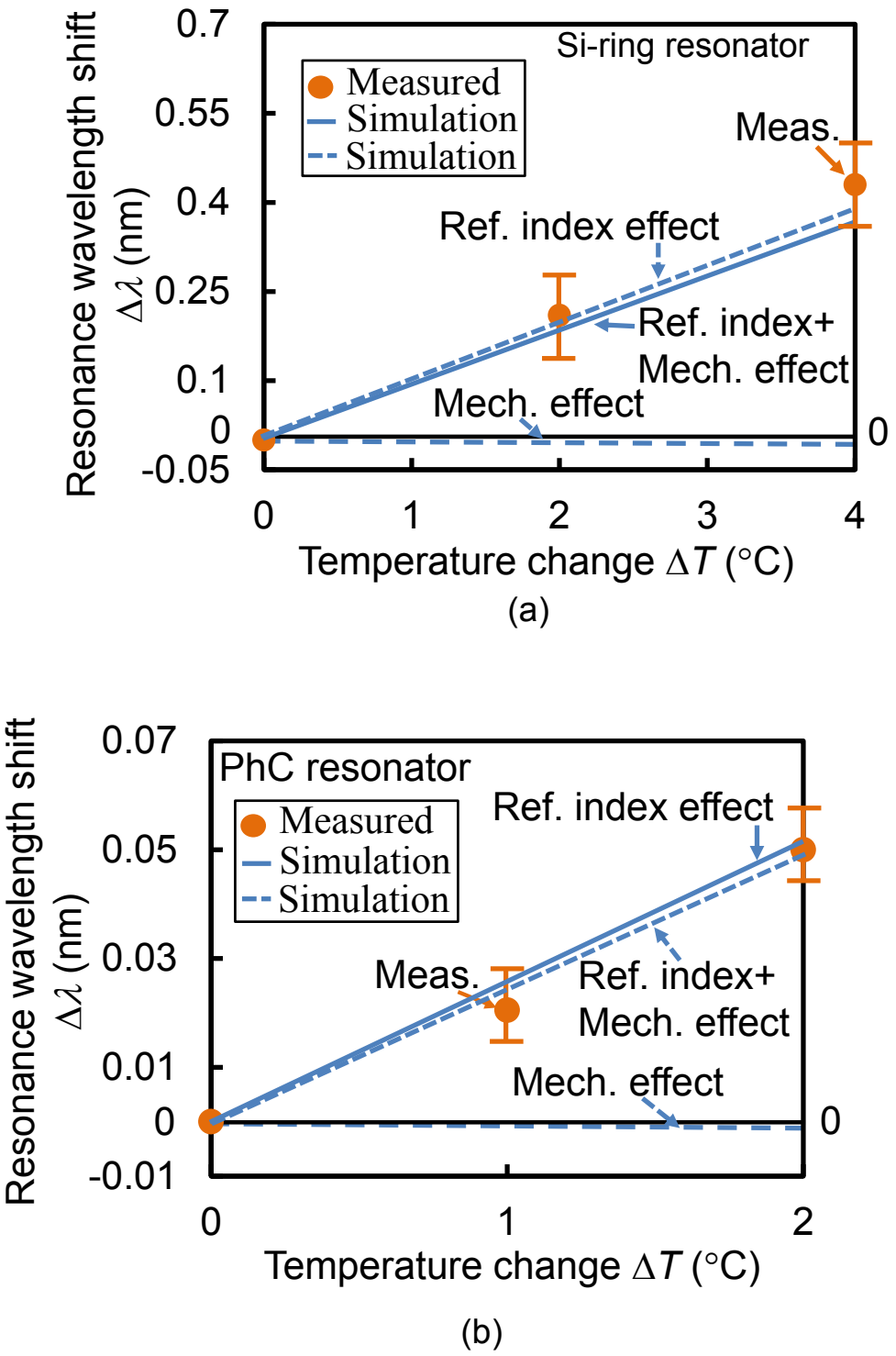

Fig 6.8. Effect of temperature on resonance wavelength shift for (a) Si ring resonator and (b) PhC cavity resonator (where silicon effective refractive index change (Ref. index effect) and mechanical effects (Mech. effect) are abbreviated).

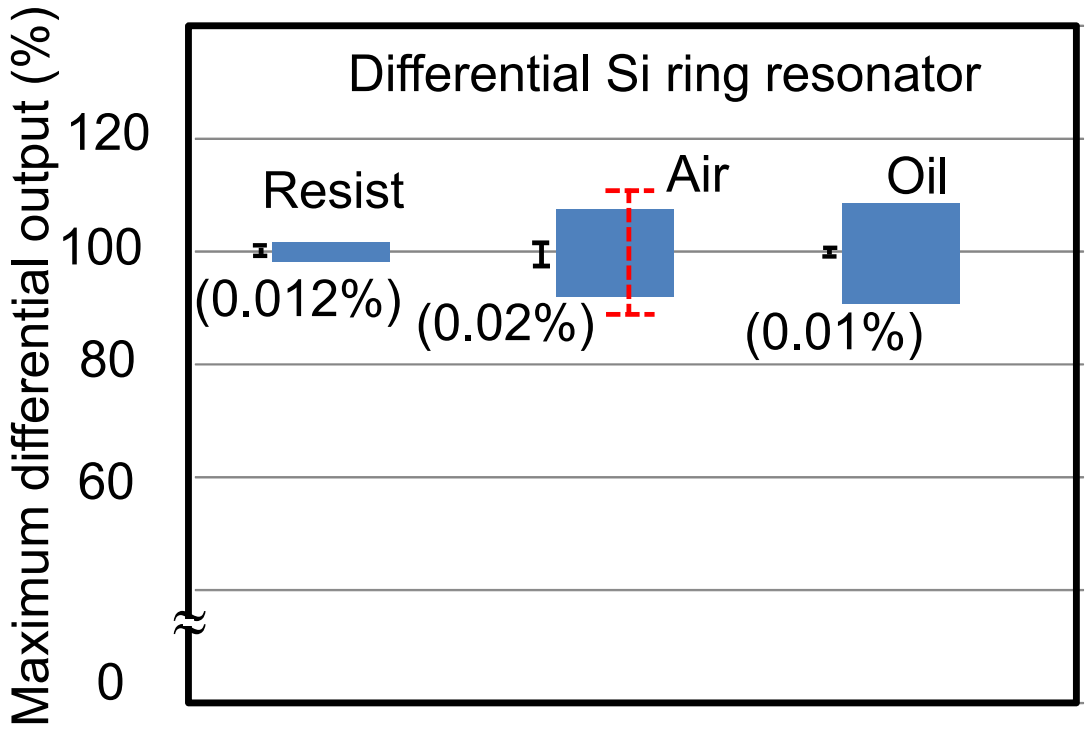

Fig 6.9. Comparison of integrated light output variation in different medium at temperature range between 25 °C and 29 °C. Measured scatter error for multiple measurements in air clad at 25 °C is expressed by ⌶ . Multiple measured scatter for resist and oil were not carried out. But similar scatter is expected for resist and oil because the scatter occurred for the measurement system error. And measured data deviation with the temperature changes (from 25 °C to 29 °C) is expressed by ▮ . Theoretical calculation for thermal change (for ΔT= 4 °C) is represent by ⌶ and the value were indicates in the parentheses.

References

[1] G. E. Jellison Jr. and H. H. Burke, J. Appl. Phys. **60** (1986) 841.

[2] J. A. McCaulley, V. M. Donnelly, M. Vernon, and I. Taha, Phys. Rev. **B 49** (1994) 7408.

[3] X. Tu, J. Song, T-Y. Liow, M. K. Park, J. Q. Yiying, J. S. Kee, M. Yu, and G-Q. Lo, Opt. Express **20** (2012) 2640.

[4] J. Teng, P. Dumon, W. Bogaerts, H. Zhang, X. Jian, X. Han, M. Zhao, G. Morthier, and R. Baets, Opt. Express **17** (2009) 14627.

[5] H. Tanobe, Y. Kondo, Y. Kadota, K. Okamoto, and Y. Yoshikuni, IEEE Photonics Tech. Lett. **10** (1998) 235.

[6] Y. Kokubun, S. Yoneda, and S. Matsuura, Elect. Lett. **34** (1998) 367.

[7] K. Maru and Y. Abe, Opt. Express **15** (2007) 18351.

[8] T. Claes, J.G. Molera, K. De Vos, E. Schacht, R. Baets, and P. Bienstman, IEEE Photonics J. **1** (2009) 197.

[9] V. R. Almeida, Q. Xu, C. A. Barrios, and M. Lipson, Opt.Lett. **29** (2004) 1209.

[10] Q. Xu, V. R. Almeida, R. R. Panepucci, and M. Lipson, Opt. Lett. **29** (2004) 1626.

[11] J.-M. Lee, D.-J. Kim, G.-H Kim, O.-K. Kwon, K.-J.Kim, and G. Kim, Opt. Express **16** (2008) 1645.

[12] X. Wang, S. Xiao, W. Zheng, F. Wang, Y. Li, Y. Hao, X. Jiang, M. Wang, and J. Yang, Opt. Comm. **282** (2009) 2841.

[13] L. Zhou, K. Kashiwagi, K. Okamoto, R. Scott, N. Fontaine, D. Ding, V. Akella, and S. Yoo, Appl. Phys. A: Materials Science & Processing **95** (2009) 1101.

[14] L. Zhou, K. Okamoto, and S. J. B. Yoo, IEEE Photonics Tech. Lett. **21** (2009) 1175.

[15] H. Huang, S.T. Ho, D. Huang, Y. Tu, H. Hu, J. Wang, and W. Liu, J. of Modern Opt. **57** (2010) 545.

[16] K. B. Gylfason, C. F. Carlborg, A. Kazmierczak, F. Dortu, H. Sohlström, L. Vivien, C. A. Barrios, W.van der Wijngaart, and G. Stemme, Opt. Express **18** (2010) 3226.

[17] Y. Atsumi, K. Inoue, N. Nishiyama, and S. Arai, Jpn. J. of Appl. Phys. **49** (2010) 50206.

[18] A. H. Harvey, J. S. Gallagher, and J. M. H. L. Sengers, J. of Phys. and Chem. Ref.

Data **27** (1998) 761.

[19] L. Eldada, Opt. Engg. **40** (2001) 1165.

[20] T. Taniguchi, Shu. Yokoyama, Y. Amemiya, T. Ikeda, A. Kuroda, and S. Yokoyama, Jpn. J. Appl. Phys. **55** (2016) 04EM04.

[21] A. K. Sana, K. Honzawa, Y. Amemiya, and S. Yokoyama, Jpn. J. Appl. Phys. **55** (2016) 04EM11.

[22] S. D. Brotherton and T. G Read, Solid State Electron. **13** (1973) 1367.

[23] W. Kern and D. A. Puotinen, RCA Rev. **31** (1970) 187.

[24] Y. Kokubun, Oyo Buturi **72** (2003) 1364 [in Japanese].

[25] Y. Kokubun and K. Kogaku (Optical Wave Engineering) (Kyoritsu, Tokyo,1999) p. 238, 297 [in Japanese].

[26] https://www-s.nist.gov/srmors/tablePDFV.cfm?tableid=181.

[27] http://www.dowcorning.com.cn/zh_CN/content/publishedlit/75-1007-01_single.pdf

[28] R. Budwing, Exp. Fluids **17** (1994) 350.

[29] D. P. Subedi, D. R. Adhikari, U. M. Joshi, H. N. Poudel, and B. Niraula, Kathma. Univ. J. of Sci., Engg. and Tech. **1** (2006) 1.

[30] A. K. Sana, M. Jun, Shu. Yokoyama, Y. Amemiya, and S. Yokoyama, "Temperature dependence of resonance characteristics of silicon resonators and thermal-stability improvement by differential operation," Jpn. J. of Appl. Phys. **56** (2017) (Accepted for publication in 2017).

Chapter 7 Conclusion

7.1 Conclusion

(1) Silicon photonic crystal resonator biosensors have been developed. We studied different type of photonic crystal based biosensors such cavity type, defect type and special type (cavity and surrounding holes are connected each other).

(2) We have demonstrated the excellent potential of light confinement of a 2D photonic crystal cavity. In particular, the cavity size greatly enhances the large wavelength shift. We measured highest Q value of $>10^5$, which is the highest value ever reported for any other photonic-crystal-based biosensors. We obtained a great improve of the sensitivity of 1570 nm=RIU. The proposed cavity-based sensor structure confirms the resonance wavelength shift with effective refractive index changes by target molecules. Also, there is a linear dependence between refractive index changes and wavelength shift.

(3) We confirm that the big cavity-type device has (more than three times) a greater wavelength shift as than the defect-type device.

(4) We succeeded in sensing the antibody–antigen reaction using photonic crystal double nanocavity resonator sensor employing PSA marker as an example target. By optimizing the immobilization of the target biomarker,

(5) We detected the PSA concentration as low as 0.01 ng/mL. Thus, our PhC based double nanocavity resonator may be promising candidate as practical biomolecules sensor in the medical diagnosis.

(6) Temperature effects on resonance wavelength shift are studied using both Si ring and photonic crystal cavity resonator type device.

(7) We reported that the temperature effects on resonance wavelength shift are dominated by the refractive index change of Si and it is demonstrated that these temperature effect is sufficiently suppressed by the differential operation. This type

of differential operation could also be applied for optical switching, modulation and so on where thermal effects should be avoided.

(8) Theoretically, we showed that the maximum differential output change for ΔT=4℃ is calculated at three different top cladding layer conditions, theoretically change for resist, air and oil are 0.012%, 0.02% and 0.01% respectively indicated

7.2 Comparison among other works

In the Table 7.1, we compared our device performance in accordance to sensitivity, Q-factor and figure of merit with other researcher work. We obtained a greatly improve the sensitivity of 1570 nm/RIU.

Table 7.1. Performance comparison of our single cavity PhC resonator device with other researcher work.

	Sensitivity, $S=\Delta\lambda/\Delta n$ (nm/RIU)	$Q=\lambda_{res/FWHM}$	Figure of merit, FOM= $S \times Q/\lambda_{res}$	Resonator type
This work	1570	10^5	$\sim 1.2 \times 10^5$	Cavity
Ref. 1	451	7000	>2000	Defect
Ref. 2	60	7000	300	Defect
Ref. 3	900	700	400	Defect

In the Table 7.2, the device performances are compared with researcher work in accordance to sensitivity, Q-factor and detection limit. We reported second smallest detection limit but a very much improved Q-factor.

Table 7.2. Performance comparison of double nanocavity PhC resonator with other researcher work.

	Sensitivity, $\Delta\lambda/\Delta n$(nm/RIU)	Quality factor, $Q=\lambda_{res}$ / FWHM	Detection limit, $DL=\lambda_{res}/QS$ (RIU)	Sensor type
This work	1571	2×10^{5}	$(4.15 \sim 4.34) \times 10^{-6}$	Double-cavity resonator
Ref. 4	500	17890	1×10^{-4}	Defect resonator
Ref. 5	132	2966	3.8×10^{-6}	Cavity resonator
Ref. 6	1500	50000	7.8×10^{-6}	Slot PhC waveguide
Ref. 7	370	7500	2.2×10^{-4}	Cavity resonator
Ref. 8	235	25000	1.1×10^{-4}	Cavity resonator

7.3 Impact of this research work

The work has impact on industry and technology where high sensitivity of detection is necessary. In the field of biosensor, photonic crystal based biosensor may play important role where several of kind biomaterial detection is necessary to knowing the public health.

The designs and demonstration of PhC cavities (cavity/defect and special shape cavity type) that have been described in this thesis have much more information for future development of high Q cavities. We studied on the cavity/defect type resonator and the size of the cavities was also studied and their effects on resonance wavelength shift. We hope that the various kind device structures certainly help to develop the high sensitivity device.

By changing the neighbor hole of the cavity or cavities there is a possibility to get better sensitivity, and high Q-factor as well.

We describe the mechanism and solution for dominating temperature effects on refractive index based Si optical resonator sensor such as ring resonator and photonic crystal resonator sensors. The temperature change affects the silicon refractive index and affects resonator mechanical shape also. As a result, it is reported that the refractive index change is dominating whereas the mechanical deformation effect is negligible. We also demonstrated that the differential operation is effective to suppress the temperature effect for Si ring resonator sensor. This type of differential operation could also be applied for optical switching, modulation and so on where thermal effects should be avoided.

The impact of this work on the engineering is the high Q-factor, high sensitivity and minimum detection limit. On the other hand, the impact on academic are the double cavity and neighbor hole radius change may have great impact on high sensitivity with minimum detection limit. We theoretically and experimentally reported that double cavity connected with radius modulated neighbor holes has great impact on Q value improvement and sensitivity as well.

References

[1] B. Wang, M. A. Dundar, R. Ntzel, F. Karouta, S. He, and R. W. Heijden, Appl. Phys. Lett. **97** (2010) 151105.

[2] L. J. Sherry, S. Chang, G. C. Schatz, and R. P. V. Duyne, Nano Lett. **5** (2005) 2034.

[3] R. Budwing, Exp. in Fluids. **17** (1994) 350.

[4] T. H. P. Chang, J. Vac. Scie. & Tech., **12** (1975) 1271.

[5] J. Zhou, H. Tian, D. Yang, Q. Liu, and Y. Ji, Opt. Comm. **330** (2014) 175.

[6] A. D. Falco, L. O'Faolain, and T. F. Krauss, Appl. Phys. Lett. **94** (2009) 063503.

[7] S. H. Mirsadeghi, E. Schelew, and J. F. Young, Appl. Phys. Lett. **102** (2013) 131115.

[8] C. Caër, S. F. Serna-Otálvaro, W. Zhang, X. L. Roux, and E. Cassan, Opt. Lett. **39** (2014) 5792.

Acknowledgement

First of all I would like to thank my supervisor Professor Shin Yokoyama for giving me a great opportunity to work with his laboratory. Without his suggestions and mentorship, the work would not have been complete ever. I appreciate his dedication during my entire PhD journey.

I am grateful to thank Professor Takamaro Kikkawa, Professor Masakazu Iwasaka, Professor Hans Juergn Mattausch, Associate Professor Anri Nakajima, Associate Professor Shin-Ichiro Kuroki, Associate Professor Tetsushi Koide and Associate Professor Tetsuo Tabei for their valuable suggestions as well as comments during my research presentation in the institute meeting.

I am thankful to Professor Akio Kuroda and Assistant Professor Takeshi Ikeda in the department of Molecular Biotechnology, Graduate School of Advanced Sciences of Matter (AdSM) for providing prostate specific antigen (PSA) biomarker and valuable discussion regarding this biomaterial in details.

I am very much grateful to Assistant Professor Yoshiteru Amemiya, in the Research Institute for Nanodevice and Bio Systems. Without his help I could not have completed my device fabrication successfully.

I would like to thank the former and current members of Professor Shin Yokoyama laboratory who helped me a lot either in my clean room or in the device characterization.

I would like to acknowledge financial support from JASSO, special scholarship from graduate school of Advanced Sciences of Matter (AdSM), research assistantship from AdSM, teaching assistantship from Research Institute for Nanodevice and Bio Systems (RNBS).

Finally, I owe my thanks to my wife Lovely Roy and daughter Adrika Aarushi Sana for being with me at all the good time and bad time as well. My PhD research could not have finished without their supports and sacrifices.

List of publications

Journal papers:

(1) Silicon photonic crystal resonators for label free biosensor
A. K. Sana, K. Honzawa, Y. Amemiya, and S. Yokoyama.
Japanese Journal of Applied Physics **55** (2016) 04EM11.

(2) Temperature dependence of resonance characteristics of Silicon resonators and thermal-stability improvement by differential operation method
A. K. Sana, M. Jun, Shu. Yokoyama, Y. Amemiya, and S. Yokoyama.
Japanese Journal of Applied Physics **56** (2017) 04CC06.

(3) High sensitivity double-cavity silicon photonic-crystal resonator for label free biosensing
A. K. Sana, Y. Amemiya, and S. Yokoyama.
Japanese Journal of Applied Physics **56** (2017) 04CM06.

Conference proceedings

(1) A. K. Sana, Ryuichi Furutani, Yoshiteru Amemiya, and Shin Yokoyama, "Mach-Zehnder Interferometer Optical Modulator with Cascaded P/N Junctions," Extended Abstracts of the 2013 International Conference on Solid State Devices and Materials, Fukuoka, 2013, pp.1004-1005.

(2) A. K. Sana,Y. Amemiya, and S.Yokoyama, "High Sensitive Biosensor using Si Photonic Crystal Cavity Resonators," Extended Abstracts of the 2015 International Conference on Solid State Devices and Materials, Sapporo, 2015, pp.380-812.

(3) A. K. Sana, Shu. Yokoyama, Y. Nakashima, Y. Amemiya, and Shin.Yokoyama, "Thermal Change in Resonance Wavelength of Si Resonator Sensors on Si on Insulator Substrate and Solution by Differential Operation," Extended Abstracts of the 2016 International Conference on Solid State Devices and Materials, Tsukuba, 2016, pp.487-488.

(4) A. K. Sana, Y. Amemiya, and S.Yokoyama, "High Sensitivity and High Quality-factor Silicon Photonic Crystal Resonator with Double Nanocavities for Label free Bio Sensing," Extended Abstracts of the 2016 International Conference on Solid State Devices and Materials, Tsukuba, 2016, pp.361-362.

(5) A. K. Sana, Y. Amemiya, T. Ikeda, A. Kuroda and S.Yokoyama, "Detection of Prostate Specific Antigen Using Silicon Photonic Crystal Nanocavity Resonator" Proc. of SPIE Vol. **10111** 1011138(1-7), San Francisco 2017 Jan. 28-Feb. 3.

公表論文
（Articles）

(1) Silicon Photonic Crystal Resonators for Label Free Biosensor
A. K. Sana, K. Honzawa, Y. Amemiya and S. Yokoyama
Japanese Journal of Applied Physics **55** 04EM11 (1-5) (2016).

(2) Temperature Dependence of Resonance Characteristics of Silicon Resonators and Thermal-Stability Improvement by Differential Operation Method
A. K. Sana, J. Maeda, Shu. Yokoyama, Y. Amemiya and S. Yokoyama
Japanese Journal of Applied Physics **56** 04CC06 (1-5) (2017).

(3) High Sensitivity Double-Cavity Silicon Photonic-Crystal Resonator for Label-Free Biosensing
A. K. Sana, Y. Amemiya and S. Yokoyama
Japanese Journal of Applied Physics **56** 04CM06 (1-5) (2017).